Time evolution of Ce as traced by APOGEE using giant stars observed with the *Kepler*, TESS and K2 missions

G. Casali[1,2], V. Grisoni[1,2], A. Miglio[1,2], C. Chiappini[3], M. Matteuzzi[1,2], L. Magrini[4], E. Willett[5],
G. Cescutti[6,7,8], F. Matteucci[6,7,8,9], A. Stokholm[1,2], M. Tailo[1], J. Montalbán[1], Y. Elsworth[5], and B. Mosser[10]

[1] Dipartimento di Fisica e Astronomia, Università di Bologna, Via Gobetti 93/2, 40129 Bologna, Italy
[2] INAF – Osservatorio di Astrofisica e Scienza dello Spazio, Via P. Gobetti 93/3, 40129 Bologna, Italy
  e-mail: giada.casali@inaf.it
[3] Leibniz – Institut fur Astrophysik Potsdam (AIP), An der Sternwarte 16, 14482 Potsdam, Germany
[4] INAF – Osservatorio Astrofisico di Arcetri, Largo E. Fermi 5, 50125 Firenze, Italy
[5] School of Physics & Astronomy, University of Birmingham, Edgbaston, Birmingham B15 2TT, UK
[6] Dipartimento di Fisica, Sezione di Astronomia, Università di Trieste, Via G. B. Tiepolo 11, 34143 Trieste, Italy
[7] INAF – Osservatorio Astronomico di Trieste, Via Tiepolo 11, 34143 Trieste, Italy
[8] INFN – Sezione di Trieste, Via A. Valerio 2, 34127 Trieste, Italy
[9] IFPU, Institute for the Fundamental Physics of the Universe, Via Beirut 2, 34151 Trieste, Italy
[10] LESIA, Observatoire de Paris, Université PSL, CNRS, Sorbonne Université, Université de Paris, 92195 Meudon, France

Received 28 February 2023 / Accepted 10 May 2023

ABSTRACT

Context. Abundances of slow neutron-capture process (*s*-process) elements in stars with exquisite asteroseismic, spectroscopic, and astrometric constraints offer a novel opportunity to study stellar evolution, nucleosynthesis, and Galactic chemical evolution.
Aims. We investigate one of the least studied *s*-process elements in the literature, cerium (Ce), using stars with asteroseismic constraints from the *Kepler*, K2, and TESS missions.
Methods. We combined the global asteroseismic parameters derived from precise light curves obtained by the *Kepler*, K2, and TESS missions with stellar parameters and chemical abundances from the latest data release of the large spectroscopic survey APOGEE and astrometric data from the *Gaia* mission. Finally, we computed stellar ages using the code PARAM with a Bayesian estimation method.
Results. We investigated the different trends of [Ce/Fe] as a function of metallicity, [α/Fe], and age taking into account the dependence on the radial position, especially in the case of K2 targets, which cover a wide galactocentric range. We finally explored the [Ce/α] ratios as a function of age in different galactocentric intervals.
Conclusions The studied trends display a strong dependence of the Ce abundances on the metallicity and star formation history. The [Ce/Fe] ratio shows a non-monotonic dependence on [Fe/H] with a peak around -0.2 dex. Moreover, younger stars have higher [Ce/Fe] and [Ce/α] ratios than older stars, confirming the latest contribution of low- and intermediate-mass asymptotic giant branch stars to the Galactic chemical enrichment. In addition, the trends of [Ce/Fe] and [Ce/α] with age become steeper moving towards the outer regions of the Galactic disc, demonstrating more intense star formation in the inner regions than in the outer regions. Cerium is thus a potentially interesting element to help constrain stellar yields and the inside-out formation of the Milky Way disc. However, the large scatter in all the relations studied here suggests that spectroscopic uncertainties for this element are still too large.

Key words. stars: abundances – Galaxy: abundances – Galaxy: evolution – stars: late-type – Galaxy: disk

1. Introduction

Our Universe is enriched in different chemical elements on different timescales (due to their different nucleosynthetic origins). This suggests that some chemical abundance ratios can be used to trace different star formation histories. One classical abundance ratio often used in Galactic archaeology is the [α/Fe] ratio (e.g. Matteucci 2021). Other abundance ratios are also expected to vary with age, for instance the ratio of slow neutron-capture process (*s*-process) to α-elements. These abundance ratios with a strong correlation with age are called chemical clocks. Recent data on open clusters (e.g. Casamiquela et al. 2021; Viscasillas Vázquez et al. 2022), and on field stars (e.g. Spina et al. 2018; Nissen et al. 2020; Morel et al. 2021) for which it was possible to measure ages have confirmed the theoretical expectations in general terms.

S-process elements can be produced in massive stars (weak component, $60 < A < 90$, with A being the atomic mass number, Pignatari et al. 2010) or in low- and intermediate-mass asymptotic giant branch (AGB) stars with a main component ($90 < A < 204$, Lugaro et al. 2003) and/or with a strong component (low-metallicity AGB stars, $204 < A < 209$, Gallino et al. 1998). Cerium (Ce) is mostly produced by the main *s*-process component ($83.5 \pm 5.9\%$ at solar metallicity, Bisterzo et al. 2014) in low-mass AGB stars ($1.5-3\,M_\odot$).

The standard view of the *s*-process in massive stars might be modified in rotating stars because of the rotational mixing operating between the H-shell and He-core during the core helium burning phase. Several observational signatures support an enhancement of *s*-process elements (up to $A \sim 140$) in massive rotating stars (Pignatari et al. 2008; Chiappini 2013; Cescutti et al. 2013; Cescutti & Chiappini 2014). Recently, an

overabundance of Ce was observed in metal-poor bulge stars (Razera et al. 2022), which was interpreted as a result of an early enrichment by fast rotating massive stars, or spinstars (Meynet & Maeder 2002; Chiappini et al. 2011; Cescutti et al. 2018).

In the last decade, [Y/Mg] and [Y/Al] have been among the most studied chemical clocks (da Silva et al. 2012; Nissen 2015; Feltzing et al. 2017; Slumstrup et al. 2017; Spina et al. 2018; Delgado Mena et al. 2019; Anders et al. 2018; Casali et al. 2020; Jofré et al. 2020; Nissen et al. 2020). However, recent works have demonstrated not only their metallicity dependence, but also the non-universality of the chemical clock–age relations, with variations in the shape of the relations at different galactocentric distances (Casali et al. 2020; Magrini et al. 2021; Casamiquela et al. 2021; Viscasillas Vázquez et al. 2022).

Owing to the large uncertainties on ages of field stars, these studies have been mostly restricted to clusters. In this context, asteroseismology comes to our aid. Through asteroseismology, we are able to detect solar-like pulsations in thousands of G-K giants using data collected by the COnvection ROtation and planetary Transits (CoRoT, Baglin et al. 2006), *Kepler* (Gilliland et al. 2010), K2 (Howell et al. 2014), and Transiting Exoplanet Survey Satellite (TESS, Ricker et al. 2014) missions. The pulsation frequencies are directly linked to the stellar structure and thus provide tight constraints on stellar properties (radius, mass, age) and evolutionary state (Chaplin & Miglio 2013).

In this paper we focus on the evolution of Ce, one of the least studied *s*-process elements in the literature, in a sample of field stars for which precise asteroseismic ages are available. The [Ce/Fe]–age (and also [Ce/α]–age) relation has been studied in open clusters and solar twins by Maiorca et al. (2011), Spina et al. (2018), Magrini et al. (2018), Delgado Mena et al. (2019), Tautvaišienė et al. (2021), Casamiquela et al. (2021), Viscasillas Vázquez et al. (2022), Sales-Silva et al. (2022), among others. They all find an increase in [Ce/Fe] with decreasing stellar age, except for Tautvaišienė et al. (2021), who find an almost flat trend.

Here we complement such studies with field stars sampling a larger age baseline than is possible with clusters alone, thanks to asteroseismic ages coming from three different missions (*Kepler*, TESS, and K2). We use Ce abundances published in the latest data release (DR17) of the high-resolution spectroscopic survey, Apache Point Observatory Galactic Evolution Experiment, APOGEE (Majewski et al. 2017; Abdurro'uf et al. 2022). Our aim is to investigate the time evolution of Ce across the Milky Way; *Kepler* and TESS are focused on the solar neighbourhood, $7.5 < R_{GC} < 8.5$ kpc, but K2 covers a large range in galactocentric radii, $4 < R_{GC} < 12$ kpc. With this dataset we investigate the [Ce/Fe] trends as a function of the metallicity [Fe/H] and [α/Fe], its time evolution, and [Ce/α] as a chemical clock.

The paper is structured as follows. In Sect. 2 we describe the data samples; in Sect. 3 we present a comparison between the Ce abundances used in this work and those determined in other surveys; in Sects. 4 and 5 we show our results for the [Ce/Fe] trends and the Ce abundance time evolution; in Sect. 6 we show a quantitative comparison of our results with Galactic chemical evolution models. Finally, in Sect. 7 we summarise and conclude.

2. Stellar samples

Our data samples combine the global asteroseismic parameters measured from light curves obtained by the *Kepler* (Borucki et al. 2010), K2 (Howell et al. 2014), and TESS (Ricker et al. 2015) missions with stellar parameters and chemi-

cal abundances inferred from near-infrared high-resolution spectra taken by the APOGEE DR17 survey (Abdurro'uf et al. 2022). These targets were then cross-matched with the Early Third Data Release of *Gaia* (*Gaia* EDR3, Gaia Collaboration 2021).

2.1. Spectroscopic constraints

The atmospheric parameters and abundances used in this paper are produced by the standard data analysis pipeline, the APOGEE Stellar Parameters and Chemical Abundances Pipeline (ASPCAP, García Pérez et al. 2016). A full description of the pipeline is given in Holtzman et al. (in prep.), and a description of an earlier implementation of this pipeline can be found in García Pérez et al. (2016).

2.2. Asteroseismic constraints

We consider three main samples. Our first data sample is composed of ~5600 *Kepler* solar-like oscillating giants whose spectroscopic parameters are available from APOGEE DR17 (Abdurro'uf et al. 2022). The list of targets and global asteroseismic constraints corresponds to the reference sample (R1) explored in Miglio et al. (2021), but updated to use photospheric parameters from APOGEE DR17.

The second data sample is composed of data collected by the TESS mission during the first year of observations in its southern continuous viewing zone (SCVZ; see Mackereth et al. 2021 for more details). The sample, which corresponds to the 'gold sample' in Mackereth et al. (2021) with APOGEE DR17 parameters available, is composed of ~1700 stars, with ~1 yr TESS observations.

The third dataset is composed of data collected by the K2 mission in 20 observational campaigns along the ecliptic. Unlike the previous two missions, K2 observed stars in a wide range of galactocentric radii crucially extending the regions sampled by *Kepler* and TESS. Atmospheric parameters from APOGEE DR17 stars are available for a total of ~11 000 stars with asteroseismic constraints from K2. For this sample we used the global parameter ν_{max}, from the Elsworth et al. (2020) pipeline, as the only asteroseismic constraint (see below for more details).

2.3. Inferring stellar masses, ages, and radii

Masses, radii, and ages are computed using the code PARAM (da Silva et al. 2006; Rodrigues et al. 2017), which makes use of a Bayesian estimation method. We input a combination of seismic indices and spectroscopic constraints, such as ν_{max}, $\Delta\nu$, [Fe/H], [α/Fe], and T_{eff}. A detailed explanation of the method is available in Miglio et al. (2021).

For the K2 dataset (80d-long light curves), however, we included as constraint the luminosity, L, instead of $\Delta\nu$, because the latter is affected by significant systematic uncertainties in shorter datasets, as described in Willett at al. (in prep.; see also Tailo et al. 2022). The luminosity is computed using the magnitude K_s from 2MASS (Skrutskie et al. 2006), distance deduced from the *Gaia* parallax, extinction determined using the `Bayestar2019` map (Green et al. 2019) through the `dustmaps` Python package (Green 2018), and bolometric corrections computed through the code by Casagrande & VandenBerg (2014, 2018a,b). In addition, the luminosity takes into account the global median *Gaia* parallax zero point offset of $-17\,\mu$as based on quasars (Lindegren et al. 2021).

When using PARAM, we considered a lower limit of 0.05 dex for the uncertainty on [Fe/H] and a limit of 50 K for T_{eff}. This choice is due to the very small uncertainties present in
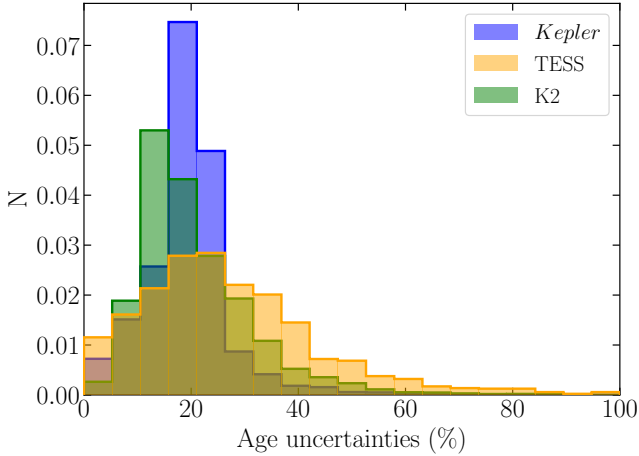
Fig. 1. Distribution of the age uncertainties for the three data samples. The area under each histogram is integrated to 1.

Fig. 2. Comparison between [Ce/Fe] using the abundances in APOGEE DR17 (this work) and the *Gaia*-ESO abundances (Randich et al. 2022). The dashed line indicates the median, whereas the solid line indicates the zero difference.

APOGEE DR17 (typical uncertainties are $\sigma_{T_{eff}} \sim 10$ K, $\sigma_{\log g} \sim 0.03$ dex and $\sigma_{[Fe/H]} \sim 0.01$ dex) as the quoted uncertainties are internal errors only, and cross-validation against other surveys shows larger systematic differences (see e.g. Rendle et al. 2019; Hekker & Johnson 2019; Anguiano et al. 2018). Moreover, model-predicted T_{eff} suffer from large uncertainties associated with the modelling of outer boundary conditions and near-surface convection, and hence we prefer to downplay the role of T_{eff}. The grid of stellar models used in PARAM for this work is the reference grid adopted in Miglio et al. (2021), labelled G2 in their work.

The distributions of uncertainties in stellar age for the three samples are shown in Fig. 1. While the longer duration of the *Kepler* time series leads to a lower median age uncertainty (20%) compared to that of TESS (28%), the relatively low median age uncertainty for K2 (18%) can be attributed to the use of a very precise (6%) luminosity instead of $\Delta \nu$. For a more detailed description on all datasets, we refer to the work by Willett et al. (in prep.).

Finally, to investigate whether using L instead $\Delta \nu$ while inferring ages could lead to a significant bias, we compared ages based on ν_{max} and L with those obtained from ν_{max} and $\Delta \nu$ for the *Kepler* and TESS samples (where $\Delta \nu$ is not affected by systematic uncertainties). As a result, we found no significant difference between the two inferred ages for the two samples (difference $\lesssim 1\sigma$).

2.4. Selection criteria

In this section we describe how we selected stars with robust spectroscopy and age estimates. Specifically, we kept stars with $S/N > 100$ and $\sigma(Ce) < 0.2$ dex. Then we removed stars with the following flags from the APOGEE survey: STARFLAG = VERY_BRIGHT_NEIGHBOR, LOW_SNR, PERSIST_HIGH, PERSIST_JUMP_POS, PERSIST_JUMP_NEG, SUSPECT_RV_COMBINATION or ASPCAPFLAG = STAR_BAD, STAR_WARN and ELEMFLAG = GRIDEDGE_BAD, CALRANGE_BAD, OTHER_BAD, FERRE_FAIL for Ce.

We also restricted the sample to stars with estimated radii smaller than $11 R_\odot$ (following the same cut present in Miglio et al. 2021). This avoids the contamination by early AGB stars and removes stars with relatively low ν_{max}, a domain where seismic inferences have not been extensively tested so far.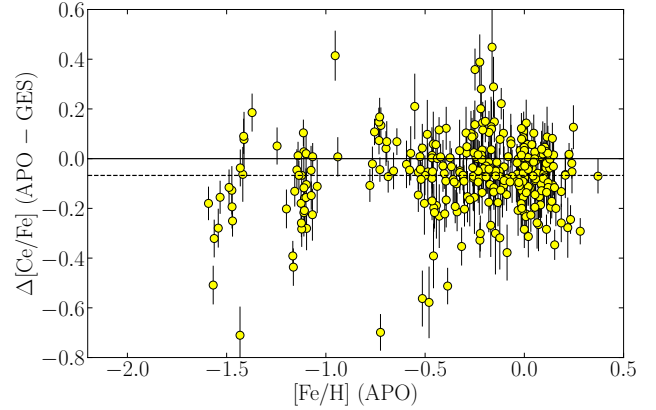 Moreover, we computed the distribution of age uncertainties over the whole population, and removed stars whose uncertainties lie in the top 5%.

Finally, the K2 sample contains very metal-poor stars with respect to those of *Kepler* and TESS. In order to have samples in the same range of metallicity, we selected stars in $-1 \leq [Fe/H] < 0.4$ dex. These selection criteria reduce the initial *Kepler* sample of ~5600 stars to ~2700, the TESS sample of ~1700 stars to ~900 and the K2 sample of ~11 000 stars to ~4000.

3. Comparison with the literature

In order to validate the Ce abundances we used in this study, we compared the stars in common between APOGEE DR17 (used in this work) and the optical counterpart from the *Gaia*-ESO DR5 survey (Randich et al. 2022). Moreover, we also compared the Ce abundances measured from APOGEE spectra using three different pipelines: ASPCAP, the standard pipeline used to obtain the abundances in the APOGEE DR17 survey, the Brussels Automatic Code for Characterizing High Accuracy Spectra (BACCHUS; Masseron et al. 2016) used in Sales-Silva et al. (2022), and its updated version for weak and blended lines, the BACCHUS Analysis of Weak Lines in APOGEE Spectra (BAWLAS) used in Hayes et al. (2022). Sales-Silva et al. (2022) redetermined the Ce abundances from the measurements of Ce II lines in the APOGEE DR16 spectra of the member stars of the open clusters present in the Open Cluster Chemical Abundances and Mapping (OCCAM) sample (Donor et al. 2020), using the BACCHUS pipeline. Hayes et al. (2022), instead, reanalysed ~120 000 APOGEE DR17 spectra with BAWLAS.

For the APOGEE DR17 sample, we selected stars with high-quality Ce abundances (the same selection in $\sigma(Ce)$, S/N, and APOGEE flags shown in Sect. 2.4). Instead, for *Gaia*-ESO, we kept stars with Ce measurements from at least two lines in their spectra. In Fig. 2 we compare the 298 stars in common between APOGEE DR17 with *Gaia*-ESO DR5. The mean difference in [Ce/Fe] is Δ[Ce/Fe](APOGEE − GES) = -0.07 ± 0.15 dex. The scatter is larger at lower metallicity (see Fig. 2).

Comparing instead the APOGEE DR17 with Sales-Silva et al. (Sales-Silva et al.), we found 162 member stars in common. They have a mean difference Δ[Ce/Fe](APOGEE − SS) of -0.13 ± 0.09 dex (see Fig. 3).

Finally, the comparison between APOGEE DR17 and Hayes et al. (2022) shows a difference of Δ[Ce/Fe](APOGEE − BAWLAS) = -0.09 ± 0.13 dex. The chemical abundance
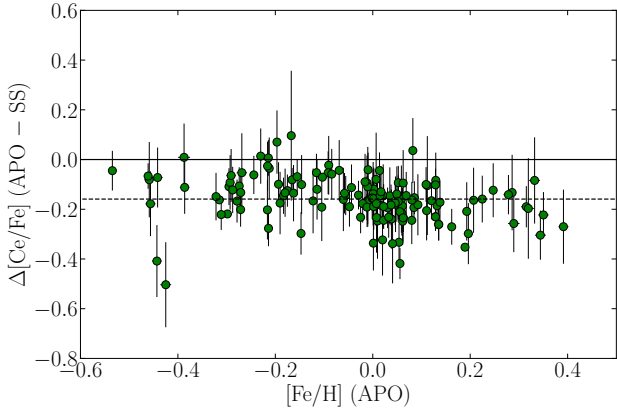
Fig. 3. Comparison between [Ce/Fe] using the abundances in APOGEE DR17 (this work) and the abundances from Sales-Silva et al. (2022). The dashed line is the median, whereas the solid line indicates the zero difference.
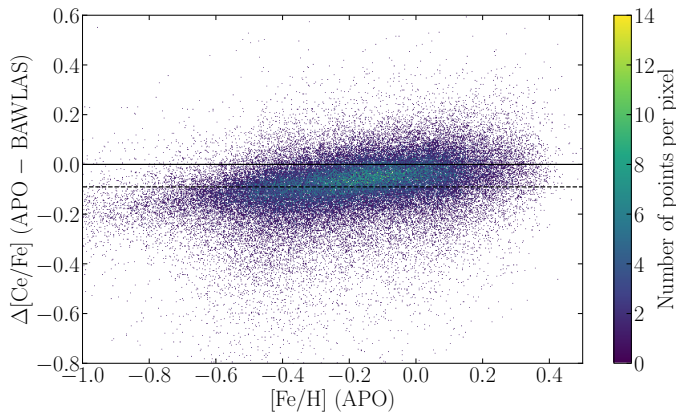

Fig. 4. Comparison between [Ce/Fe] using the abundances in APOGEE DR17 (this work) and the BAWLAS abundances (Hayes et al. 2022). The dashed line is the median, whereas the solid line indicates the zero difference.

patterns of Ce from ASPCAP and BAWLAS are relatively similar. However, Hayes et al. (2022) find a trend in the differences between the two Ce measurements as a function of [Fe/H] at lower metallicities. Figure 4 shows the density plot of the Δ[Ce/Fe](APOGEE − BAWLAS) for 94 522 stars in common. This metallicity-correlated offset seems to primarily be a result of using different $T_{\rm eff}$ and $\log g$, calibrated for ASP-CAP and uncalibrated for BAWLAS. Nevertheless, the stars in our sample do not cover these metallicities, so we can overlook this trend.

In all these cases, the measurements from APOGEE DR17 show a systematic offset of ~0.1 dex with a larger scatter at lower metallicity. This offset may be due to the different pipelines, spectral range, and linelists used in the different surveys. Moreover, the uncertainties on the Ce abundance present in the APOGEE DR17 survey are larger than the uncertainties from the analyses in the *Gaia*-ESO survey, in Sales-Silva et al. (2022), and in Hayes et al. (2022; see their distributions in Fig. 5). Despite a large standard deviation of the Ce abundance differences among the samples, we can conclude that the measurements from the APOGEE DR17 show a rather good agreement with the *Gaia*-ESO, Sales-Silva et al. (2022), and Hayes et al. (2022) studies.
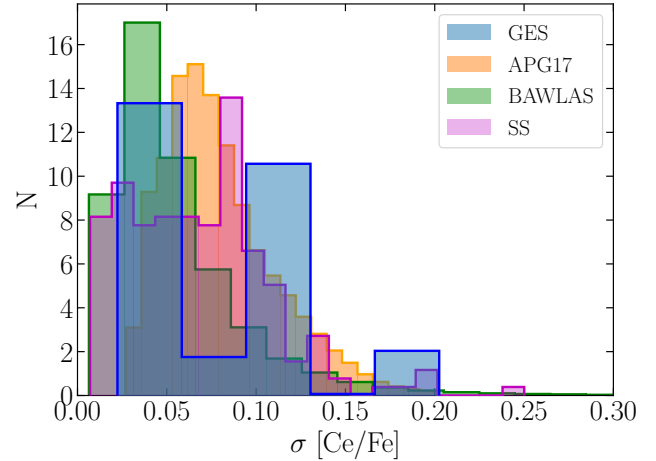

Fig. 5. [Ce/Fe] uncertainty distributions in APOGEE DR17, Sales-Silva et al. (2022), Hayes et al. (2022), and *Gaia*-ESO DR5.

Open clusters. To understand whether the use of the BAWLAS pipeline can provide an advantage to our work with respect to ASPCAP, we computed the mean and standard deviation of [Ce/Fe] for the member stars of open clusters in common between the two pipelines. The list of the open clusters and the catalogue of their members can be found in Myers et al. (2022). The values are shown in Fig. 6. We can see that the average values of [Ce/Fe] computed with the BAWLAS results are larger than those computed with ASPCAP, except in a few cases. This discrepancy is related to the offset that we discussed in the previous section. In both pipelines, the standard deviation is large ($\sigma \sim 0.1$ dex) for almost all clusters, showing a spread in the Ce measurements among the member stars of the same cluster, which is not expected since they should be homogeneous. Such large standard deviations indicate that the Ce uncertainties are likely underestimated by both pipelines. Moreover, our results are similar using one or the other pipeline. Therefore, we chose to use the ASPCAP results for the following section.

4. The [Ce/Fe] abundance ratio trends

In this section we show the *Kepler*, TESS, and K2 stars selected following the criteria presented in Sect. 2.4. These samples contain stars with a distribution in age and metallicity spanning [0, 14] Gyr and [−1,+0.4] dex, respectively. In addition, we removed outliers using a Huber regression (Huber 1964), with a hyperparameter set to 3.

In the next subsections we present two different planes to present the samples: [Ce/Fe]–[α/M] and [Ce/Fe]–[Fe/H].

4.1. [Ce/Fe] versus [α/M]

Figure 7 shows the [Ce/Fe]–[α/M] for our three datasets, colour-coded by age. We used the ASPCAP [α/M] as a proxy for [α/Fe]. In our dataset the difference between [α/M] and an average [α/Fe] defined using O, Mg, Si, S, and Ca over Fe is negligible (with a mean offset equal to −0.002 dex and a standard deviation of 0.016 dex). In all datasets, we have two samples of stars that display two stellar populations: the low-α sequence ([α/M] ≲ 0.15 dex) and the high-α sequence ([α/M] ≳ 0.15 dex). The number of high-α stars is larger for the K2 sample and lower for the TESS sample. Additionally, the high-α sequence also contains the oldest stars in all three samples with a mean age
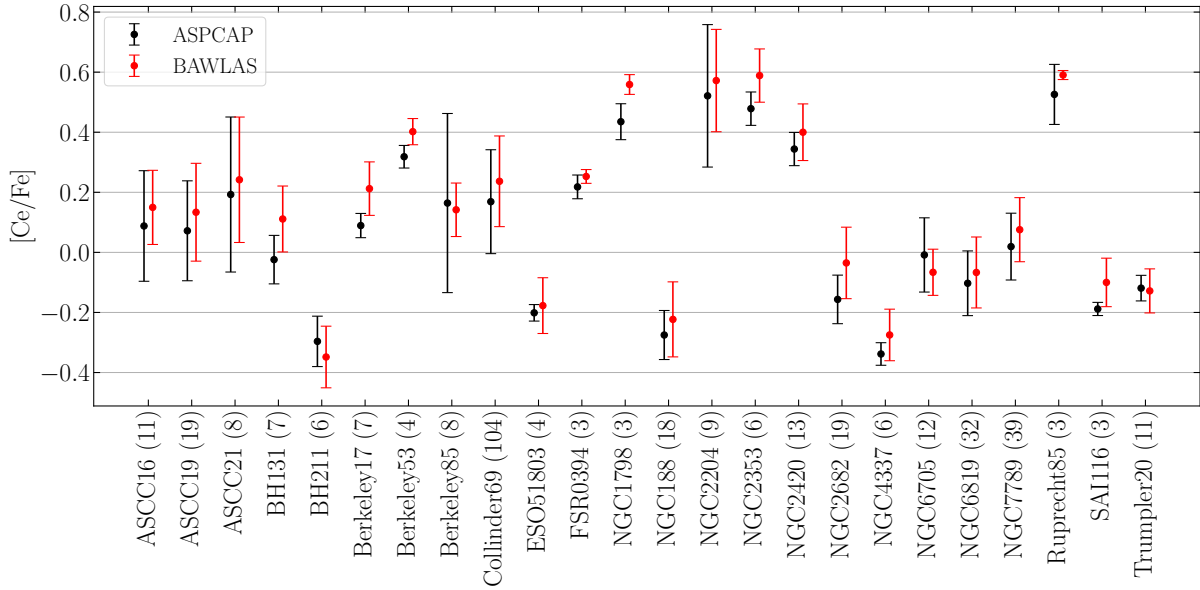
Fig. 6. Mean and standard deviation of [Ce/Fe] for the open clusters in common between ASPCAP (black) and BAWLAS (red) pipelines. The [Ce/Fe] mean in each cluster is represented with a dot and the standard deviation with the error bar. The number near the cluster names represents the number of stars in each cluster.

~10−11 Gyr (see e.g. Miglio et al. 2021 for the age of the high-α population). The other sequence, instead, spans a large range in the stellar age, and with a gradient in age with increasing [Ce/Fe] and [α/M]. Finally, the high-α sequence has an average of [Ce/Fe] around −0.2 dex, while the low-α sequence has an average of [Ce/Fe] around −0.1 dex.

In the next sections we focus on the low-α sequence since low- and intermediate-mass AGB stars polluted mainly this stellar population. Moreover, it is more numerous with respect to the high-α sequence, and allows us to compare our field stars with open clusters present in the literature (e.g. Sales-Silva et al. 2022; Viscasillas Vázquez et al. 2022; Casamiquela et al. 2021). Furthermore, we did not make a selection in z, the height on the Galactic plane, because this cut would remove the old stars from our samples.

Here we adopted a separation in [α/M], using a piece-wise function to divide the populations. The function is an adjustment of the separation curve proposed by Adibekyan et al. (2012) for our data:

$$[\alpha/\mathrm{M}] = \begin{cases} 0.15 & [\mathrm{Fe/H}] \leq -0.3 \\ -0.34 \cdot [\mathrm{Fe/H}] + 0.05 & -0.3 < [\mathrm{Fe/H}] \leq 0 \\ 0.05 & [\mathrm{Fe/H}] > 0 \end{cases} \quad (1)$$

We chose this division following the most-adopted functions to separate low- and high-α sequences present in the literature (see e.g. Adibekyan et al. 2012; Mikolaitis et al. 2014).

4.2. [Ce/Fe] versus [Fe/H] in the low-α sequence

In Fig. 8 we show the [Ce/Fe] trend in the low-α sequence as a function of metallicity for the three samples. They show the same shape: an increasing [Ce/Fe] at increasing [Fe/H] with a maximum at ~−0.2 dex in [Fe/H], and a drop in [Ce/Fe] at higher metallicities. The stars are also colour-coded by stellar age. At a given metallicity, the younger field stars show a [Ce/Fe] content that is larger than the older stars. A better visualisation of this trend is shown in the histograms in Fig. B.1. These histograms display the [Ce/Fe] binned in different ranges of stellar ages.

The peaks of the histograms move towards lower [Ce/Fe] with increasing age.

A similar behaviour is also shown in the samples of open clusters present in Viscasillas Vázquez et al. (2022) and Sales-Silva et al. (2022). In the former, they analyse 62 open clusters observed by the *Gaia*-ESO DR5 survey, while in the latter, they study 42 open clusters observed by the APOGEE DR16 survey (with spectral analysis using BACCHUS).

As described in the introduction, the predominant fraction of s-process elements, such as Ce, is produced by long-lived stars (1.5−3.0 $M_\odot$; see e.g. Cristallo et al. 2009, 2011). This, together with the secondary nature (dependence on metallicity) of the s-process elements, determines the behaviour shown in the figure. Chemical evolution models present in literature (Prantzos et al. 2018; Grisoni et al. 2020; the three-infall model in Contursi et al. 2023) show a banana shape with a rise in [Ce/Fe], a peak, and then a decline, similar to that seen in Fig. 8.

In addition, the s-process production of Ce in AGB stars is strongly dependent on the metallicity (Busso et al. 2001; Vescovi et al. 2020). It depends on the number of iron nuclei as seeds for the neutron captures and on the flux of neutrons. The former decreases with decreasing metallicity, while the latter increases because it depends (approximately) on $^{13}\mathrm{C}/^{56}\mathrm{Fe}$, which increases with decreasing metallicity ($^{13}\mathrm{C}$ is a primary element, and does not depend on metallicity). This means there are more neutrons per seed in low-metallicity AGB stars and fewer in high-metallicity AGB stars. Therefore, stellar evolution models predict lower [Ce/Fe] in higher-metallicity AGB stars (Cristallo et al. 2015; Karakas & Lugaro 2016; Battino et al. 2019), implying the trend that we see in Fig. 8.

5. Time evolution of Ce abundance in the low-α sequence

In this section we study the temporal evolution of the Ce abundance in the low-α sequence. We explore the [Ce/Fe] and [Ce/α] trends as a function of age and position in the Galactic disc.

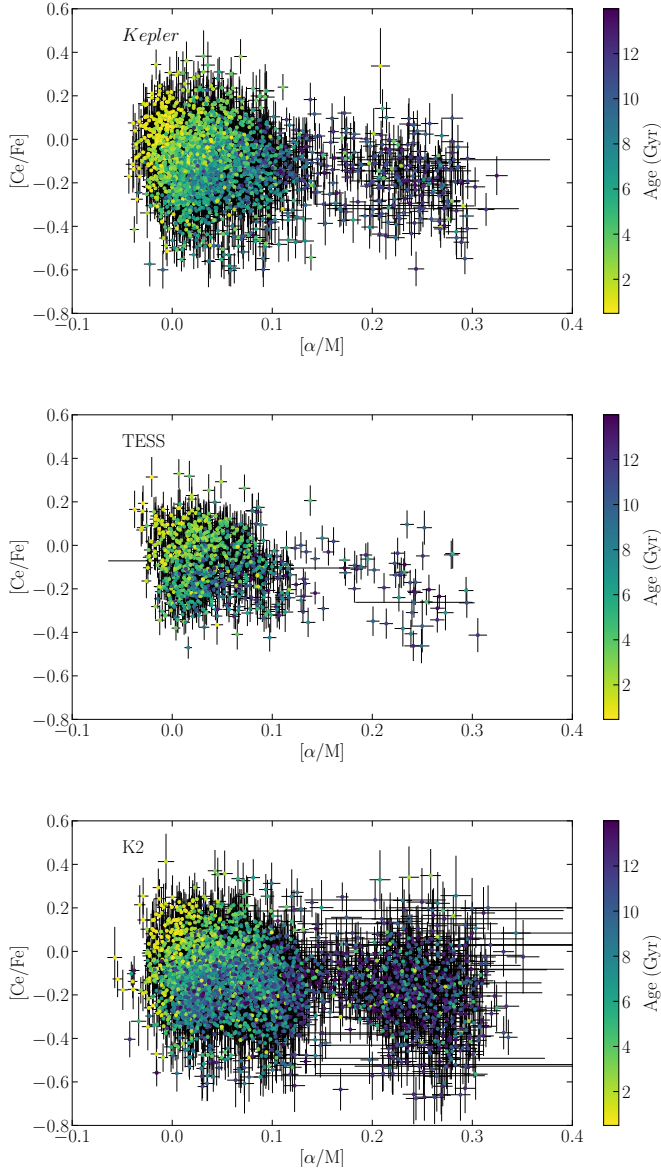**Fig. 7.** [Ce/Fe] vs. [α/M]. Shown are *Kepler* (top panel), TESS (middle panel), and K2 (bottom panel) stars. The stars are colour-coded by stellar age.

Fig. 8. [Ce/Fe] vs. [Fe/H] in low-α sequence. Shown are *Kepler* (top panel), TESS (middle panel), and K2 (bottom panel) stars. The stars are colour-coded by stellar age.

5.1. [Ce/Fe] versus age

Figure 9 shows the correlation of [Ce/Fe] with stellar age for our three samples, colour-coded by metallicity. The three lines in the figure represent the mean [Ce/Fe] in three different bins of [Fe/H]: [Fe/H] < −0.1, −0.1 ≤ [Fe/H] ≤ 0.1, [Fe/H] > 0.1 dex. These three lines clearly illustrate the metallicity dependence of the [Ce/Fe]–age relation. In particular, at a given age metal-poor stars have a higher [Ce/Fe] ratio than the metal-rich stars. Moreover, [Ce/Fe] increases with decreasing age, and becomes almost flat for ages older than 6 Gyr. The same behaviour is shown in Sales-Silva et al. (2022) for the open clusters. However, in this figure and in the work of Sales-Silva et al. (2022), the location of the stars in the Galactic disc is not taken into account.

The majority of our stars are located in the solar neighbourhood (7.5 < R_{GC} < 8.5 kpc). Nonetheless, they could have come from the inner or outer regions of the Galactic disc and transited in the solar vicinity, or could have migrated in previous epochs due to the change in their eccentricity through radial
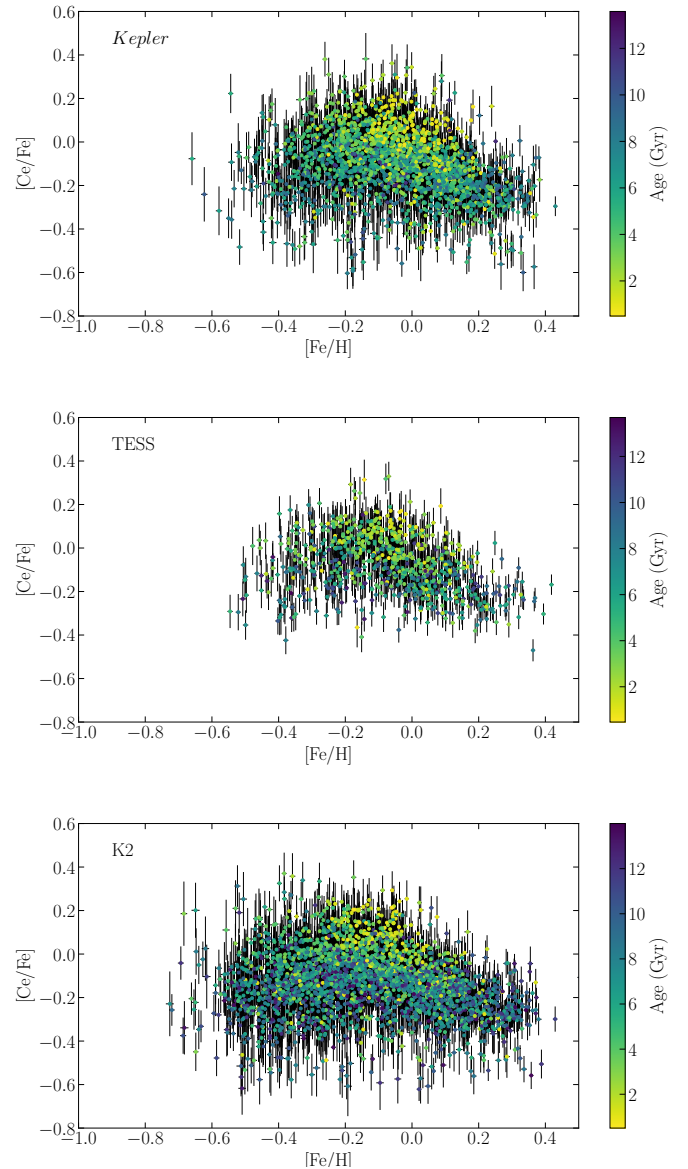
heating or in their angular momentum. To better understand their provenance, we can compute the guiding radius R_g, which is the radius of a circular orbit with specific angular momentum L_z. Moreover, the adoption of R_g instead of the galactocentric radius R_{GC} can mitigate the blurring effect due to epicyclic oscillations around the guiding radius (Schönrich & Binney 2009). However, it cannot overcome the migrating effect due to the churning, which can change R_g due to interactions with spiral arms or bars (Sellwood & Binney 2002; Binney & Tremaine 2008).

The guiding radius is computed from the stellar orbits obtained using the GalPy package of Python, in which the model MWpotential2014 for the gravitational potential of the Milky Way is assumed (Bovy 2015). Through the astrometric information by *Gaia* EDR3, distances from Bailer-Jones et al. (2021), an assumed solar galactocentric distance $R_0 = 8$ kpc, a height above the plane $z_0 = 0.025$ kpc (Jurić et al. 2008), a circular velocity at the solar galactocentric distance equal to $V_c = 220\,\text{km s}^{-1}$, and the Sun's motion with respect to the local standard of
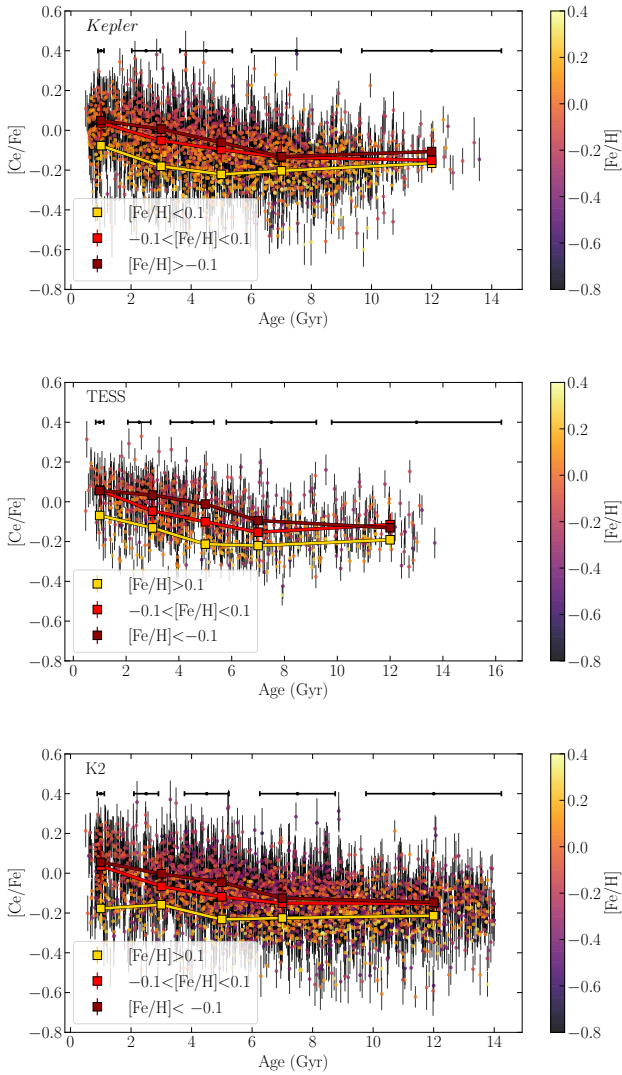
Fig. 9. [Ce/Fe] vs. stellar age for the three samples. The data are colour-coded by metallicity. The three lines represent the [Ce/Fe] mean in different bins of metallicity and age. The error budget of stellar age is shown at the top of each panel.

Fig. 10. Distribution of R_g of the three selected samples.

Through a Markov chain Monte Carlo (MCMC) procedure we derived the posterior distributions of the parameters of the fitting m_1, c, n_1, and k, where k is the switch point of the fitting line. In our model we took into account the uncertainties on [Ce/Fe] and stellar age. We also included in our calculation an intrinsic scatter of the relation, ϵ.

In this procedure, we used uniform priors for m_1, c, n_1, k, and ϵ, with limits for k ($4 < k < 10$ Gyr) and ϵ ($\epsilon > 0$). We ran the simulation with 10 000 samples, 1000 of which are used for burn-in. The script is written in Python using the `emcee` package (Foreman-Mackey et al. 2013).

In order to decide if the broken-line was the best model for our data, we compared a broken-line and a single-line given the data by computing the Bayesian information criterion (BIC). The model with the lowest BIC is generally the most reasonable one. In the bins with R_g larger than 7 kpc, the broken-line provides a lower BIC, while in the bins of $R_g < 7$ kpc for the *Kepler* and TESS samples and $R_g < 5$ kpc for the K2 sample, the single-line provides the lowest BIC. For the range $5 \le R_g < 7$ kpc of the K2 sample, the broken-line provides a marginally lower BIC than the single-line. In each region we adopted the model with the lowest BIC.

The convergence of the Bayesian inference is checked against the traces of each parameter and their auto-correlation plots. The spread (68% confidence interval plus intrinsic scatter) of the models resulting from the posteriors are represented in Fig. 11 with the red shaded area, while their values are reported in Table 1.

The [Ce/Fe] trends in the three samples show different behaviours, in particular in the young regime, between inner and outer regions. The latter usually have higher [Ce/Fe] than the former at a given age (the slope is more negative; see the second column on Table 1). Moving towards the outer regions the [Ce/Fe]–age trends become increasingly steep in all our datasets. Dividing the samples by guiding radius makes it clear that there is a strong dependence of the [Ce/Fe] abundances on the location of the stars. The behaviour of [Ce/Fe] with R_g seems to be complex and likely related to different star formation histories and to metallicity dependency of the stellar yields.

In more detail, the left panels of Fig. 11 ($R_g < 7$ kpc) show a large fraction of *Kepler* and K2 stars coming from the inner disc with respect to the TESS stars. Moreover, the trends of [Ce/Fe] with stellar age in these bins of R_g are quite flat, with a slope of ~ -0.01 dex Gyr^{-1} against the slopes in the outer regions of ~ -0.02, ~ -0.03 dex Gyr^{-1}. These trends could be due to the

rest $[U_\odot, V_\odot, W_\odot] = [11.1, 12.24, 7.25]$ km s^{-1} (Schönrich et al. 2010), we obtained the orbital parameters, among which the guiding radius R_g. The distribution of R_g of the three datasets is shown in Fig. 10. The K2 sample shows a larger distribution with respect to those of *Kepler* and TESS; those of the latter are located between $5 \lesssim R_g \lesssim 10$ kpc, while K2 reaches $R_g \sim 4$ kpc in the inner disc and $R_g \sim 12$ kpc in the outer disc, as expected from the different field locations and distances reached.

Figure 11 shows the same plane of Fig. 9 for the *Kepler*, TESS and K2 samples, divided in three different bins of guiding radius: $R_g < 7$ kpc, $7 \le R_g \le 8$ kpc, $R_g > 8$ kpc. Since K2 has a larger range in R_g with respect to *Kepler* and TESS (see Fig. 10), we added two more bins for this dataset, not covered by the other two data samples: $R_g < 5$ kpc and $R_g > 10$ kpc.

In order to visualise in a more quantitative way the different trends in the different bins and the flattening at old age, we modelled the distribution of [Ce/Fe] versus stellar age through a broken-line as follows:

$$[\text{Ce/Fe}] = \begin{cases} m_1 \cdot \text{Age} + c, & \text{Age} \le k \\ n_1 \cdot (\text{Age} - k) + (m_1 \cdot k + c), & \text{Age} > k. \end{cases} \quad (2)$$
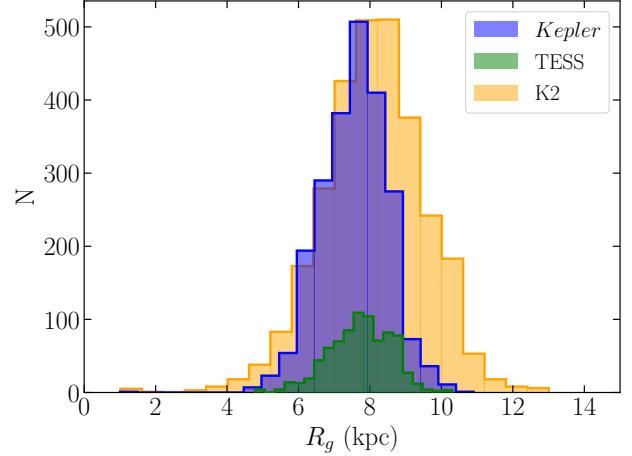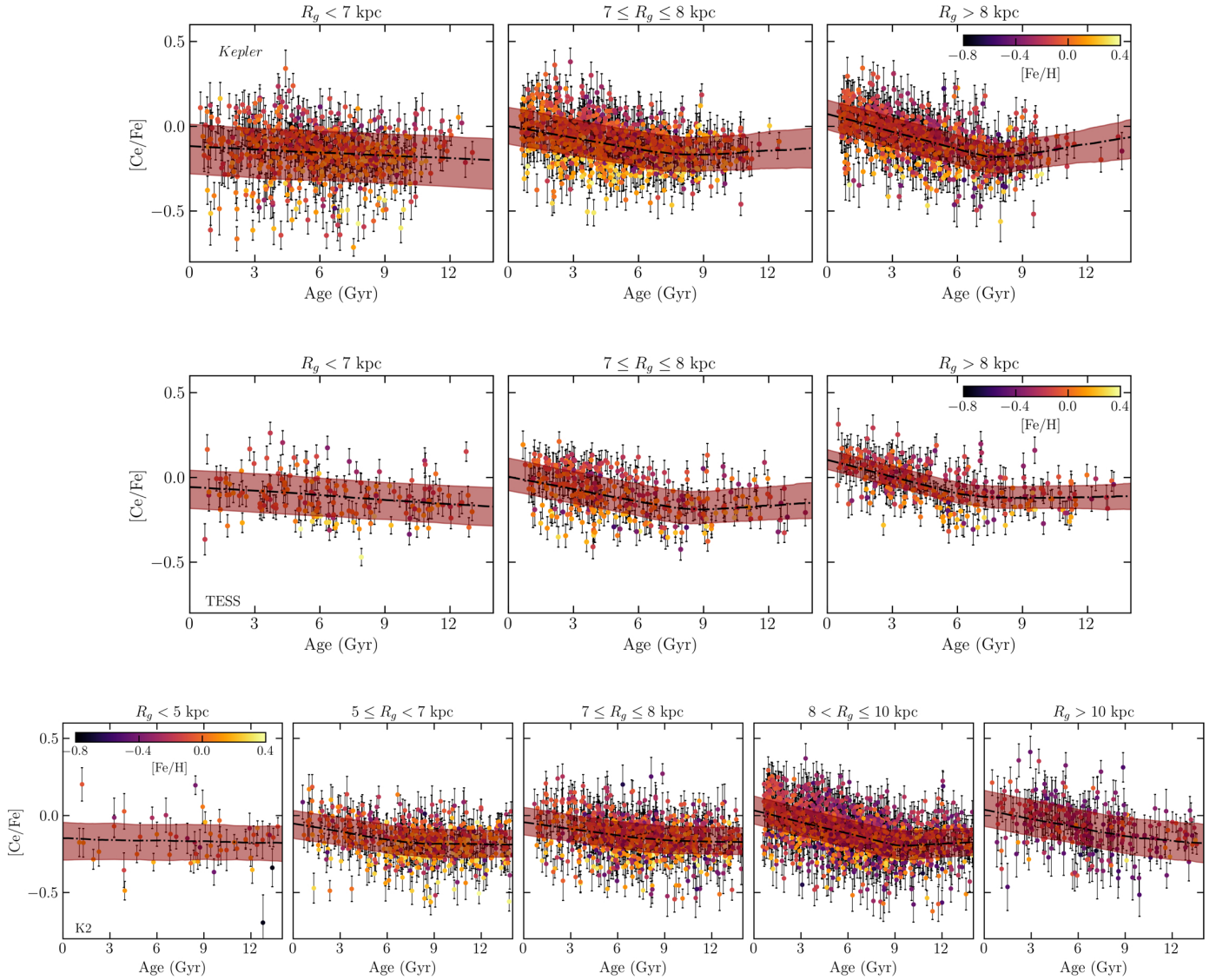
Fig. 11. [Ce/Fe] vs. stellar age in different bins of R_g. The *Kepler* sample is shown in the upper panel, the TESS sample in the middle panel, and the K2 one in the bottom panel. The data are colour-coded by metallicity. The dash-dotted line represents the best fit, and the shaded area the 68% confidence interval plus intrinsic scatter.

more intense star formation efficiency (SFE) in the inner regions of the Galactic disc, where high values of [Ce/Fe] are reached at earlier epochs.

In the other panels with $R_g > 7$ kpc, there is a clear increasing trend with decreasing age. The slope in the young regime becomes steeper towards the outer regions ($R_g > 8$ kpc) in all datasets. In the solar vicinity and outer disc, where the star formation rate is less intense with respect to the inner regions, the increasing trends with decreasing age can be due to the recent contribution of low- and intermediate-mass AGB stars to the Galactic enrichment. Instead, the flattening of the slope at ages older than 6–8 Gyr (see the parameter k in Table 1) might reflect the lower contribution of low- and intermediate-mass AGB stars in early epoch of Galaxy formation because they have not yet started to contribute significantly. We also tested whether the flattening of the data in the oldest regime could be due to their larger uncertainties on age. We generated mock data with a distribution similar to ours, an uncertainty of 30% on age, and an intrinsic scatter of 0.05 dex using a single-line model (see Appendix A). Applying the same MCMC procedure as for the

two models (broken-line and single-line), we obtained a lower BIC for the single-line. This suggests that the flattening is not a consequence of the larger uncertainties on the oldest age, but a consequence of the Galactic chemical evolution.

5.2. [Ce/α] as a chemical clock

The ratios of *s*-process elements to α-elements are widely studied as age indicators because they show a steeper trend with age than [*s*/Fe]. In this section we investigate [Ce/α]–age trends for the low-α sequence stars in the *Kepler*, TESS, and K2 samples in the same R_g bins shown in Sect. 5.1. The α-elements we take into account in this work are the same as studied by Sales-Silva et al. (2022) for their open clusters: O, Mg, Si, and Ca. In this way we can compare the trends present in our low-α sequence stars with their open clusters.

In order to study the [Ce/α] trends in a more quantitative way, we modelled their distributions at different R_g, also taking into account the [Fe/H] dependence (following the work by Delgado Mena et al. 2019; Casali et al. 2020;

Table 1. Parameters of the MCMC fitting for the [Ce/Fe]–age relations in the *Kepler*, TESS, and K2 samples.

Bin	m_1 (dex/Gyr)	c (dex)	n_1 (dex/Gyr)	k (Gyr)	ϵ (dex)
			Kepler		
$R_g < 7$ kpc	-0.006 ± 0.002	-0.122 ± 0.016	–	–	0.139 ± 0.005
$7 \leq R_g \leq 8$ kpc	-0.022 ± 0.003	0.007 ± 0.011	$0.005^{+0.013}_{-0.009}$	$7.6^{+0.9}_{-0.9}$	0.099 ± 0.004
$R_g > 8$ kpc	-0.035 ± 0.003	0.071 ± 0.011	0.018 ± 0.012	$7.6^{+0.4}_{-0.6}$	0.086 ± 0.005
			TESS		
$R_g < 7$ kpc	-0.008 ± 0.003	-0.062 ± 0.023	–	–	0.104 ± 0.008
$7 \leq R_g \leq 8$ kpc	-0.025 ± 0.004	0.016 ± 0.016	$0.008^{+0.012}_{-0.010}$	$7.9^{+1.0}_{-0.8}$	0.095 ± 0.006
$R_g > 8$ kpc	-0.034 ± 0.004	0.101 ± 0.016	$0.0005^{+0.012}_{-0.008}$	$6.8^{+1.3}_{-0.9}$	0.065 ± 0.007
			K2		
$R_g < 5$ kpc	-0.001 ± 0.005	-0.158 ± 0.047	–	–	0.110 ± 0.017
$5 \leq R_g < 7$ kpc	-0.015 ± 0.004	-0.058 ± 0.019	0.000 ± 0.004	$7.93^{+0.93}_{-1.38}$	0.088 ± 0.005
$7 \leq R_g \leq 8$ kpc	-0.015 ± 0.003	-0.044 ± 0.017	-0.004 ± 0.004	$7.85^{+1.51}_{-1.38}$	0.099 ± 0.004
$8 < R_g \leq 10$ kpc	-0.025 ± 0.002	0.043 ± 0.009	0.006 ± 0.006	$9.18^{+0.49}_{-0.52}$	0.097 ± 0.003
$R_g > 10$ kpc	-0.020 ± 0.005	0.050 ± 0.003	$-0.009^{+0.012}_{-0.008}$	$8.14^{+1.4}_{-2.5}$	0.115 ± 0.008

Viscasillas Vázquez et al. 2022) as follows:

$$[Ce/\alpha] = \begin{cases} m_1 \cdot \text{Age} + m_2 \cdot [Fe/H] + c, & \text{Age} \leq k \\ n_1 \cdot (\text{Age} - k) + (m_1 \cdot k + c + m_2 \cdot [Fe/H]), & \text{Age} > k \end{cases}$$

(3)

In our calculation, we also took into account the uncertainties on [Ce/α], [Fe/H], and stellar age. We adopted a single-line for the bin of $R_g < 7$ kpc for *Kepler* and TESS and the bin of $R_g <$ 5 kpc for K2 where their BIC is lower.

The best fits with the spread (68% confidence interval plus intrinsic scatter) of the models resulting from the posteriors are represented in Figs. 12 and 13 with a black line and a red shaded area. Their values are shown in Table 2.

The [Fe/H] colour-coding of these stars show a dependence on metallicity. We can see that stars with lower metallicity have higher [Ce/α] at a given age. Furthermore, the stars at higher metallicity show an almost flat trend with respect to the metal poor ones (see Fig. B.2 for a better visualisation of these trends). The same behaviour is displayed by Sales-Silva et al. (2022) and Viscasillas Vázquez et al. (2022) for their samples of open clusters.

This result was already shown in Feltzing et al. (2017), Delgado Mena et al. (2019), Casali et al. (2020), and Magrini et al. (2021) for [Y/α]. Casali et al. (2020), Magrini et al. (2021), and Viscasillas Vázquez et al. (2022) suggested that the metallicity dependence is due to the different star formation history and the non-monotonic dependence of s-process yields on [Fe/H]. In particular, Magrini et al. (2021) investigated the different metallicity dependence of s-process AGB yields if we include or not the magnetic-buoyancy-induced mixing (Vescovi et al. 2020). This mixing can cause a change in the metallicity dependence of the s-process production due to a change in the ^{13}C pocket in AGB stars, specifically for metal-rich stars in the inner regions. Therefore, the s-process yields including the mixing are lower than s-process yields without mixing. This scenario is a signature of the complexity of the s-process yields and, consequently, of the chemical evolution models of these elements. For this reason, a comparison between the observed age versus chemical composition trends, and predictions from chemical evolution models can help us to understand the Ce production in our Galaxy.

Moreover, looking at the [Ce/α]–age relations at different R_g, it is clear how their slopes become steeper moving towards the outer regions: m_1 becomes more negative with increasing R_g (see Table 2). This behaviour is a suggestion of the late enrichment of Ce in the Galaxy evolution due to the low- and intermediate-mass AGB stars and indicates a [Ce/α] gradient in the Galactic disc. Moreover, there is a flattening at the oldest ages, a trend hinted at by Sales-Silva et al. (2022) for all studied α-elements. However, we have the advantages of exploiting a homogeneous sample of stars with precise age, spanning the entire range in age and a large interval in metallicity. This is not possible using open clusters because they have ages typically younger than 7 Gyr and metallicity in the range [−0.4, +0.4] dex.

To conclude, the [Ce/α] trends with stellar age, metallicity, and R_g are consistent in all data samples within 3σ. The slight difference among the fitting parameters, particularly for K2, is likely due to the selection effects: our K2 targets have a broader z distribution (where z is the height from the Galactic mid-plane) with respect to the *Kepler* and TESS targets. For a given R_g bin, stars in K2 are located, on average, at greater distances from the Galactic plane. This different z distribution implies a different distribution in age since stars with higher z are older. A larger number of old stars in the K2 sample can slightly change the fitting parameters with respect to the TESS and *Kepler* datasets.

Application to field stars. The chemical clock relations obtained from a sample of stars with well-known ages (e.g. stars with asteroseismic age) are usually applied to other field stars of which we know the abundances, but we cannot derive age using standard techniques (e.g. isochrone fitting, asteroseismology). There are some examples in the literature, for instance Casali et al. (2020) and Viscasillas Vázquez et al. (2022) for the [s-/α] ratios, but also Casali et al. (2019), Masseron & Gilmore (2015), Martig et al. (2016), and Ness et al. (2016) for [C/N].

Unfortunately, the large spread in the Ce abundances does not permit us to apply the relations in Table 2 to a sample of field stars. At a given age, there are stars with a difference in [Ce/α] of the order of 0.5 dex, and the intrinsic scatter of these relations is of the order of ∼0.1 dex. Part of this scatter can be ascribed to radial migration. By using R_g we can mitigate the scatter associated with the blurring effect alone, not accounting for churning.
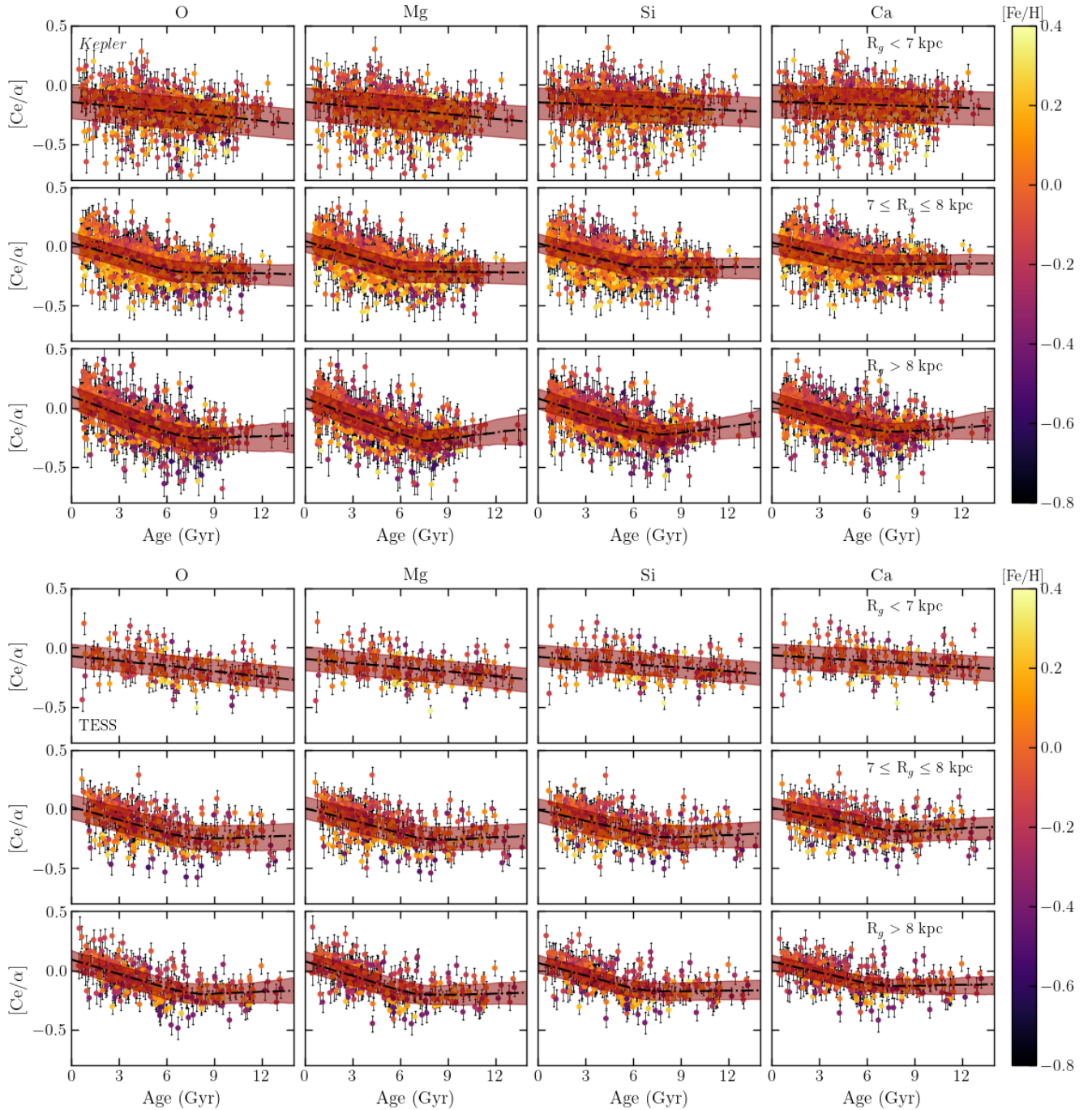
Fig. 12. [Ce/α]–age planes for *Kepler* (top panels) and TESS (bottom panels). The points are colour-coded by [Fe/H]. The black dash-dotted line represents the best fit, and the red shaded area the 68% confidence interval plus intrinsic scatter.

To consider the full effect of radial migration, we would need to estimate the birth radii of stars (e.g. by interpolating the position of the stars in the age–metallicity relation in comparison with the chemical evolution curves for each radius from the models). In this way the scatter would most likely be reduced. Nevertheless, this treatment is beyond the scope of this work.

In addition to the expected scatter due to radial migration, there is also the fact that additional scatter is due to Ce measurement uncertainties. The uncertainties on the Ce abundances are likely underestimated, as is the case for most of the uncertainties on other abundances and atmospheric parameters in APOGEE DR17. This is also proved by the large standard devi-

ation in the average abundances of star clusters in the Sect. 3. A better treatment of the Ce uncertainties might reduce the intrinsic scatter in the model and make these chemical clock relations useful to be applied to samples of field stars. We tested the sum in quadrature of the mean of the standard deviations measured for the open clusters shown in Fig. 6 ($\sigma \sim 0.1$ dex) to Ce uncertainties. The result is a significant reduction of the intrinsic scatter ($\sim$50%) of the relations, while the fit parameters remain unaltered.

All these sources of scatter make impossible to apply the [Ce/α]-[Fe/H]-age relations to derive the 'chemical age' of other field stars. Furthermore, the [Ce/α]–age trends become flat for age >6 Gyr, so this chemical clock cannot be applied to old stars.
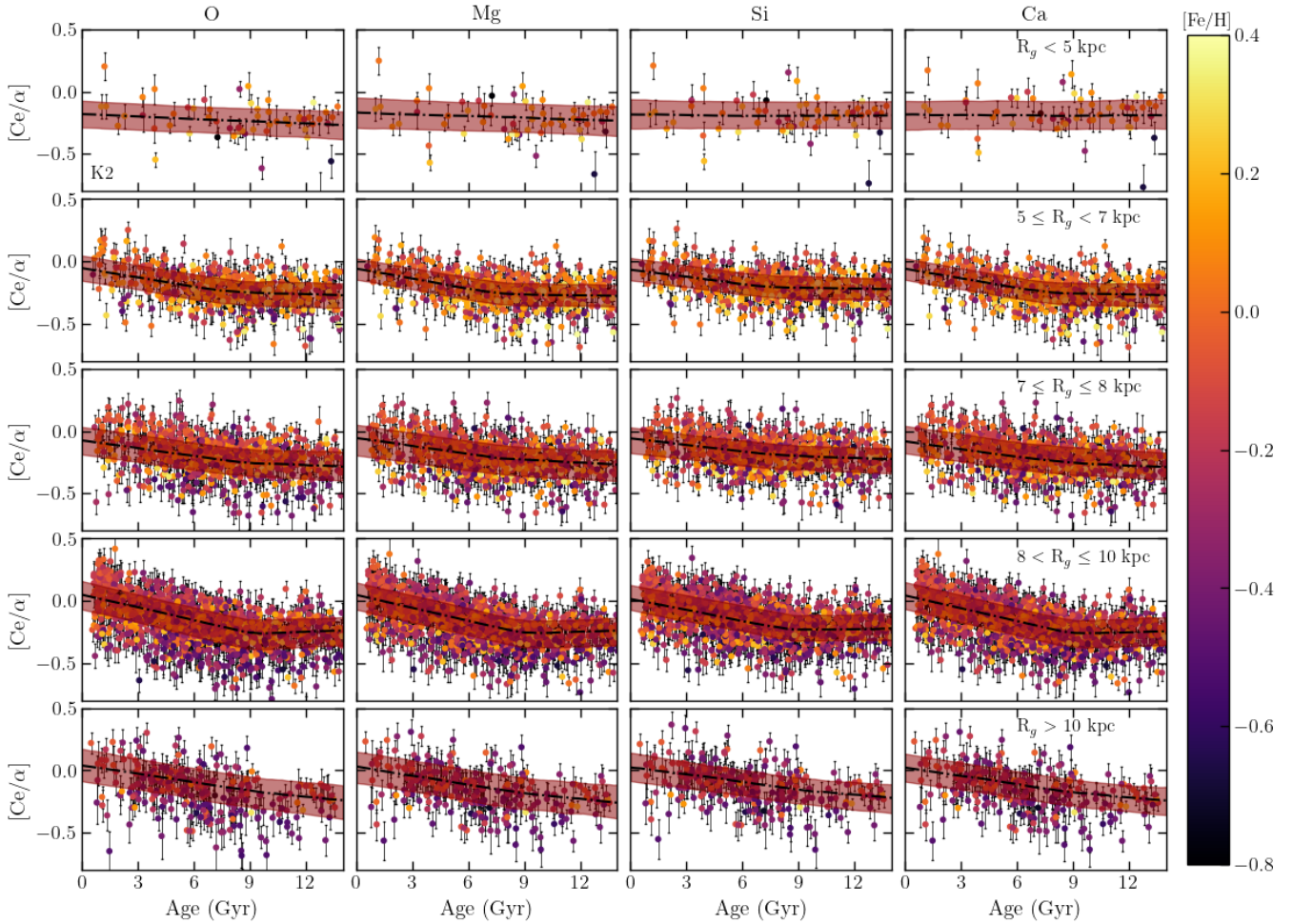
Fig. 13. [Ce/α]–age planes for the K2 sample. The symbols are the same as in Fig. 12.

6. Comparison with Galactic chemical evolution models

Here we interpret our observational results in the light of chemical evolution models, showing in particular the effect of different star formation efficiencies on the chemical evolution of Ce. A more quantitative analysis on Galactic chemical evolution (GCE) models and radial migration effects will be given in a future paper.

We compared the [Ce/α] trends with the predictions of a GCE model. We focused on the [Ce/O] ratio since O is the most representative α-element with the highest percentage of production from Type II Supernovae.

We considered the reference model of Grisoni et al. (2017, 2020) to follow the evolution of the Galactic thin disc. In this model Ce is produced by both the s- and r-process. Low- and intermediate-mass AGB stars in the range 1.3−6 $M_\odot$ are responsible for most of the s-process, and the corresponding yields are taken from the database FRUITY (Cristallo et al. 2009, 2011). Moreover, we also included the s-process contribution from rotating massive stars, considering the nucleosynthesis prescriptions of Frischknecht et al. (2016) for these stars. The r-process yields for Ce are obtained by scaling the Eu yields adopted in Cescutti & Chiappini (2014), according to the abundance ratios observed in r-process-rich stars (Sneden et al. 2008). For core-collapse supernovae we considered the yields of Kobayashi et al. (2006).

In Fig. 14 we show the observed and predicted [Ce/O] versus age in different bins of R_g, where Ce and O have different timescales of production, with Ce being mainly produced by low-mass AGB stars and O by massive stars. The predictions are for the reference model of the Galactic thin disc (Grisoni et al. 2020), with three different star formation histories, reference case A (SFE = 0.5 Gyr^{-1}), and model B (SFE = 0.2 Gyr^{-1}) and model C (SFE = 0.1 Gyr^{-1}) for the less efficient star formation efficiency. In order to better understand the fundamental contribution of AGB stars for the Ce production, we also show the model without AGB contribution. This shows a lower limit, where the contribution to the Ce abundance derives from the massive stars only. The chemical evolution of Ce is very sensitive to the star formation history since the yields of Ce are very dependent on mass and metallicity. By assuming a more efficient star formation history (case A in Fig. 14), we obtained a faster chemical evolution, reaching high values of [Ce/O] at earlier epochs; the slope [Ce/O] versus age then flattens. Instead, a milder star formation history shows an increase in [Ce/O] towards younger ages, due to the fact that AGB stars contribute at later times with respect to the massive ones.

Because of the large scatter due to the uncertainties on the Ce measurements and to stellar radial migration, the three models A, B, and C can only be used to describe the trends of our data in each bin of guiding radius. Model A represents better the [Ce/O] trend in the inner regions, while the models with a milder SFE (model B and C) describes the [Ce/O]

Table 2. Parameters of the MCMC fitting for the [Ce/α]–[Fe/H]-age relations in the *Kepler*, TESS, and K2 samples.

| Ratio	m_1 (dex/Gyr)	m_2	c (dex)	n_1 (dex/Gyr)	k (Gyr)	ϵ (dex)
			Kepler			
			$R_{\rm g} < 7$ kpc			
[Ce/O]	-0.013 ± 0.002	-0.074 ± 0.036	-0.136 ± 0.015	–	–	0.135 ± 0.005
[Ce/Mg]	-0.011 ± 0.002	-0.132 ± 0.037	-0.147 ± 0.015	–	–	0.136 ± 0.005
[Ce/Si]	-0.006 ± 0.002	-0.140 ± 0.038	-0.151 ± 0.016	–	–	0.137 ± 0.005
[Ce/Ca]	-0.004 ± 0.002	-0.126 ± 0.035	-0.145 ± 0.016	–	–	0.136 ± 0.005
			$7 \le R_{\rm g} \le 8$ kpc			
[Ce/O]	-0.039 ± 0.003	-0.177 ± 0.024	0.038 ± 0.013	-0.004 ± 0.007	6.1 ± 0.6	0.086 ± 0.004
[Ce/Mg]	-0.041 ± 0.004	-0.211 ± 0.025	0.040 ± 0.013	-0.002 ± 0.007	6.1 ± 0.6	0.087 ± 0.004
[Ce/Si]	-0.034 ± 0.003	-0.229 ± 0.023	0.026 ± 0.012	-0.001 ± 0.005	5.9 ± 0.6	0.083 ± 0.004
[Ce/Ca]	-0.032 ± 0.004	-0.192 ± 0.022	0.027 ± 0.013	0.000 ± 0.005	5.7 ± 0.6	0.082 ± 0.004
			$R_{\rm g} > 8$ kpc			
[Ce/O]	-0.052 ± 0.005	-0.023 ± 0.031	0.103 ± 0.015	0.002 ± 0.020	$6.9^{+1.0}_{-1.2}$	0.096 ± 0.005
[Ce/Mg]	-0.050 ± 0.004	-0.049 ± 0.029	0.082 ± 0.013	0.015 ± 0.020	$7.3^{+0.5}_{-1.2}$	0.088 ± 0.005
[Ce/Si]	-0.042 ± 0.004	-0.067 ± 0.028	0.071 ± 0.012	0.016 ± 0.017	$7.4^{+0.4}_{-0.9}$	0.083 ± 0.005
[Ce/Ca]	-0.037 ± 0.006	-0.049 ± 0.029	0.057 ± 0.017	0.010 ± 0.019	$7.2^{+0.7}_{-1.9}$	0.083 ± 0.005
			TESS			
			$R_{\rm g} < 7$ kpc			
[Ce/O]	-0.014 ± 0.003	-0.118 ± 0.059	-0.075 ± 0.022	–	–	0.101 ± 0.009
[Ce/Mg]	-0.013 ± 0.003	-0.154 ± 0.057	-0.091 ± 0.022	–	–	0.098 ± 0.009
[Ce/Si]	-0.011 ± 0.003	-0.163 ± 0.055	-0.077 ± 0.021	–	–	0.095 ± 0.008
[Ce/Ca]	-0.008 ± 0.003	-0.154 ± 0.055	-0.064 ± 0.022	–	–	0.097 ± 0.008
			$7 \le R_{\rm g} \le 8$ kpc			
[Ce/O]	-0.035 ± 0.004	-0.056 ± 0.042	0.015 ± 0.017	0.003 ± 0.011	$7.6^{+0.6}_{-0.7}$	0.102 ± 0.007
[Ce/Mg]	-0.035 ± 0.004	-0.104 ± 0.039	0.008 ± 0.017	0.006 ± 0.011	$7.7^{+0.6}_{-0.7}$	0.099 ± 0.006
[Ce/Si]	-0.031 ± 0.004	-0.110 ± 0.038	-0.003 ± 0.017	0.004 ± 0.009	7.5 ± 0.7	0.093 ± 0.006
[Ce/Ca]	-0.027 ± 0.004	-0.096 ± 0.038	0.013 ± 0.016	0.006 ± 0.010	$7.6^{+0.7}_{-0.8}$	0.088 ± 0.006
			$R_{\rm g} > 8$ kpc			
[Ce/O]	-0.040 ± 0.004	-0.013 ± 0.044	0.084 ± 0.018	0.004 ± 0.015	$7.3^{+0.9}_{-1.1}$	0.079 ± 0.007
[Ce/Mg]	-0.041 ± 0.005	-0.036 ± 0.038	0.085 ± 0.018	$0.001^{+0.013}_{-0.009}$	$6.8^{+0.9}_{-0.8}$	0.077 ± 0.007
[Ce/Si]	-0.035 ± 0.004	-0.068 ± 0.037	0.065 ± 0.017	$0.002^{+0.011}_{-0.008}$	$6.7^{+1.6}_{-0.8}$	0.068 ± 0.007
[Ce/Ca]	-0.030 ± 0.004	-0.044 ± 0.033	0.070 ± 0.016	0.001 ± 0.007	$6.6^{+1.0}_{-0.8}$	0.058 ± 0.007
			K2			
			$R_{\rm g} < 5$ kpc			
[Ce/O]	-0.006 ± 0.005	0.141 ± 0.075	-0.183 ± 0.047	–	–	0.113 ± 0.017
[Ce/Mg]	-0.004 ± 0.005	-0.017 ± 0.075	-0.181 ± 0.047	–	–	0.115 ± 0.017
[Ce/Si]	-0.001 ± 0.005	-0.045 ± 0.074	-0.182 ± 0.047	–	–	0.109 ± 0.017
[Ce/Ca]	-0.000 ± 0.005	0.059 ± 0.074	-0.171 ± 0.048	–	–	0.110 ± 0.017
			$5 \le R_{\rm g} < 7$ kpc			
[Ce/O]	-0.025 ± 0.020	-0.002 ± 0.004	-0.056 ± 0.017	-0.004 ± 0.005	8.077 ± 0.005	0.091 ± 0.026
[Ce/Mg]	-0.026 ± 0.020	-0.031 ± 0.004	-0.059 ± 0.017	-0.002 ± 0.005	7.863 ± 0.005	0.089 ± 0.026
[Ce/Si]	-0.019 ± 0.020	-0.072 ± 0.004	-0.066 ± 0.017	-0.003 ± 0.005	7.434 ± 0.004	0.083 ± 0.023
[Ce/Ca]	-0.026 ± 0.020	-0.031 ± 0.004	-0.059 ± 0.017	-0.002 ± 0.006	7.836 ± 0.005	0.089 ± 0.025
			$7 \le R_{\rm g} \le 8$ kpc			
[Ce/O]	-0.020 ± 0.003	0.079 ± 0.025	-0.061 ± 0.017	-0.007 ± 0.005	8.298 ± 1.382	0.114 ± 0.005
[Ce/Mg]	-0.021 ± 0.003	0.001 ± 0.024	-0.067 ± 0.017	-0.008 ± 0.005	7.913 ± 1.333	0.109 ± 0.004
[Ce/Si]	-0.018 ± 0.003	-0.017 ± 0.023	-0.061 ± 0.017	-0.006 ± 0.004	7.395 ± 1.259	0.101 ± 0.004
[Ce/Ca]	-0.021 ± 0.003	0.001 ± 0.025	-0.066 ± 0.017	-0.008 ± 0.005	7.926 ± 1.342	0.109 ± 0.004
			$8 < R_{\rm g} \le 10$ kpc			
[Ce/O]	-0.035 ± 0.002	0.136 ± 0.021	0.047 ± 0.011	0.004 ± 0.007	8.992 ± 0.496	0.111 ± 0.004
[Ce/Mg]	-0.034 ± 0.002	0.059 ± 0.020	0.034 ± 0.011	0.004 ± 0.006	8.931 ± 0.469	0.103 ± 0.004
[Ce/Si]	-0.029 ± 0.002	0.018 ± 0.019	0.022 ± 0.010	0.003 ± 0.006	8.812 ± 0.553	0.100 ± 0.004
[Ce/Ca]	-0.034 ± 0.002	0.061 ± 0.019	0.035 ± 0.011	0.004 ± 0.006	8.916 ± 0.482	0.104 ± 0.004
			$R_{\rm g} > 10$ kpc			
[Ce/O]	-0.024 ± 0.007	0.204 ± 0.057	0.035 ± 0.034	-0.018 ± 0.011	7.827 ± 2.335	0.125 ± 0.009
[Ce/Mg]	-0.024 ± 0.006	0.128 ± 0.054	0.029 ± 0.031	-0.014 ± 0.011	8.172 ± 2.082	0.112 ± 0.009
[Ce/Si]	-0.021 ± 0.006	0.109 ± 0.051	0.033 ± 0.030	-0.015 ± 0.010	7.881 ± 2.316	0.108 ± 0.008
[Ce/Ca]	-0.024 ± 0.006	0.128 ± 0.054	0.026 ± 0.031	-0.014 ± 0.012	8.181 ± 2.165	0.112 ± 0.009
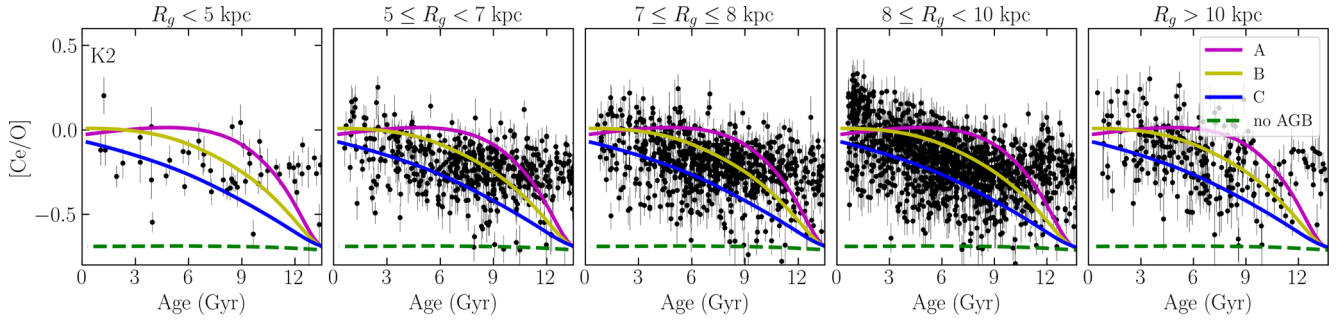
Fig. 14. Observed and predicted [Ce/O] vs. age for the K2 sample in five bins of R_g. The Galactic chemical evolution models are labelled as follows: A for the most efficient star formation history, B and C for the less efficient star formation histories, and the dashed line for the model without AGB star contribution.

behaviour in the outer regions, as expected also from the inside-out scenario (Matteucci & Francois 1989; Chiappini et al. 2001; Grisoni et al. 2018; Spitoni et al. 2021). In agreement with the inside-out scenario, we assume that the inner Galactic regions form more quickly than the outer ones: in this way, the larger number of stars per unit time in the inner regions reaches the maximum [Ce/O] value earlier with respect to the outer regions, which evolve with a milder SFE. To conclude, the inside-out scenario, combined with the metallicity dependence of AGB yields, can explain the findings discussed in the previous sections.

Moreover, the increasing trends of the observed [Ce/O] moving towards the outer regions is a possible signature of a [Ce/O] gradient in the Galactic disc. This gradient is made less clear because of the large scatter of the data. The reason for this scatter could be related to the uncertainties of the Ce measurements and radial migration. Even though we used the R_g to mitigate the blurring effect, there is still the churning component, which makes the study of abundance gradients in the Galactic disc very complicated. The treatment of the radial migration is beyond the scope of this work, but we can overcome this problem by focusing on the youngest ages (<1 Gyr). It is expected that radial migration does not affect young stars (or at least only slightly) because they have not had time to migrate yet.

In Fig. 15 we plot the K2 stars with age <1 Gyr, which is the age bin least affected by radial migration[1]. There is still scatter in this age bin, but we can see a [Ce/O] gradient in the data. The fit is shown in the figure and is compared with the points at the present time of the GCE model at different galactocentric distances (Grisoni et al. 2018) and the intercepts of the MCMC models shown in Table 2 at different bins of radii. The linear regression is obtained using a MCMC simulation. We can see good agreement between the fit of the data with the gradient predicted by models at the present time. Nevertheless, the spread of the linear regression is very large. Our goal is neither to give a robust theoretical explanation of these trends nor to study in detail the gradients at this stage, but to present the results from an observational point of view.

7. Summary and conclusions

The study of the abundance trends of s-process elements in our Galaxy is very important for constraining theoretical models. Thanks to the data collected by the *Gaia* mission; by large spectroscopic surveys such as *Gaia*-ESO, GALAH, and APOGEE;

---

[1] See Anders et al. (2017) who found the metallicity gradients for CoRoT stars younger than 1 Gyr to be similar to the value traced by Cepheids and HII regions.
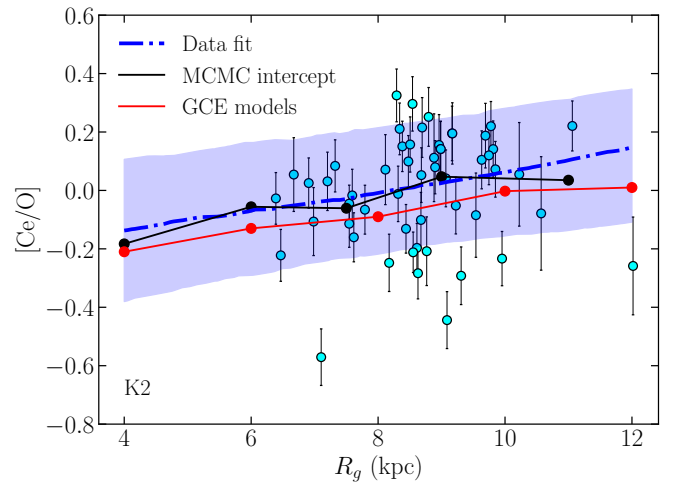

Fig. 15. [Ce/O] gradient for K2 stars with age < 1 Gyr (cyan circles). The blue dashed line represents the best fit and the blue shaded area the 68% confidence interval plus intrinsic scatter. The black line is the intercept of the MCMC simulation studied in Table 2 at the present time in the five R_g bins; the red line the GCE models at the present time at 4, 6, 8, 10, and 12 kpc.

and space missions such as *Kepler*, TESS, K2, and CoRoT, we can start exploiting the orthogonal constraints offered by age and chemistry to infer the history of s-process elements, and consequently the formation and evolution of the Milky Way.

In this work we focus on the heavy s-process element Ce for three different datasets: *Kepler*, TESS SCVZ, and K2. For all of them, we have abundances from the APOGEE DR17, where Ce is the only measured s-process element in this survey. Currently, APOGEE is the only high-resolution large spectroscopic survey that can be cross-matched with the TESS and *Kepler* dataset.

The TESS and *Kepler* samples observed stars in the solar neighbourhood, while K2 observed different regions of our Galaxy, spanning a wide range of galactocentric distances. Furthermore, using these three datasets of field stars, we were able to cover the oldest age, not covered by open clusters (see e.g. Sales-Silva et al. 2022; Casamiquela et al. 2021; Viscasillas Vázquez et al. 2022) and benefit from the improved statistics of a larger sample. Open clusters can cover ages up to 7 Gyr, with the bulk of them around 1 Gyr. Finally, the number of observed (spectroscopically) open clusters is less than ~150 (see e.g. open clusters in the *Gaia*-ESO survey, OCCAM, OCCASO, Randich et al. 2022; Myers et al. 2022; Casamiquela et al. 2016).

In this study, we investigated the [Ce/Fe] abundance ratio trends and the temporal evolution of Ce. Here are our main findings:

- In the [Ce/Fe]–[α/M] plane we see how the two population with high- and low-α content have different ages and a different average [Ce/Fe]. The high-α sequence contains older stars with lower mean [Ce/Fe], while the low-α sequence displays a wide range of stellar ages with higher mean [Ce/Fe]. We focused on the low-α sequence only since the low- and intermediate-mass AGB stars polluted mainly this stellar population.

- In the [Ce/Fe]–[Fe/H] plane we see a peak in [Ce/Fe] ratio at around -0.2 dex in [Fe/H] with a consequent decrease in [Ce/Fe] towards lower and higher metallicity. This is related to a non-monotonic metallicity dependence of the s-process stellar yields, and a decreasing efficiency of the s-process at high metallicity. Moreover, at a given [Fe/H], younger stars have a higher [Ce/Fe] content than the older stars. A similar behavoiur is studied in open clusters by Sales-Silva et al. (2022) and Viscasillas Vázquez et al. (2022), among others.

- To study the time evolution of Ce, we divided the samples in different bins of guiding radius R_g. The [Ce/Fe]–age plane shows how metal-poor stars have a higher [Ce/Fe] content than metal-rich stars at a given age in all bins of R_g. Stars with $R_g < 7$ kpc show a flattening trend with age. This is a possible signature of the high SFE in the inner regions. In the other bins of R_g ($R_g > 7$ kpc), [Ce/Fe] decreases with increasing age with a different slope. Moreover, for ages $< 6-8$ Gyr the trend is steeper, while for ages $> 6-8$ Gyr the trend is almost flat, confirming the results for open clusters in Sales-Silva et al. (2022). This is a possible signature of the latest enrichment of low-mass AGB stars for Ce (i.e. the inside-out scenario), combined with metal-dependent AGB yields. This late enrichment takes a few Gyr to pollute the interstellar medium. Furthermore, the [Ce/Fe]–age slope becomes steeper and steeper moving towards the outer regions.

- Then, we studied the [Ce/α] as a chemical clock for the low-α sequence in the same bins of R_g. The ratio of Ce to an α-element maximises the correlation with the stellar age. The trend is decreasing with age, showing that younger stars have a higher content of [Ce/α] than the older ones. Moreover, we can see different behaviours at different metallicities, as we already saw in the literature, and a change in slope at 6–8 Gyr for these ratios. As we have already seen for [Ce/Fe]–age, the [Ce/α]–age trends also show a steeper slope in the young regime moving towards the outer disc. However, the large scatter due to the underestimate of the Ce uncertainties and radial migration does not allow us to apply the [Ce/α]-age-[Fe/H] relations to date stars for which we cannot derive age with other stellar age dating methods.

- Finally, we compared the [Ce/O]–age relations with the predictions of Galactic chemical evolution models. This comparison supports the interpretation that the [Ce/O] trends with R_g seen in the observational data, but also [Ce/α] in general, are indeed related to the evolution of the Galactic disc: the observed behaviour is in agreement with the metallicity dependence of the AGB yields and the inside-out scenario, where the inner parts of the Galaxy form more quickly than the outer ones. GCE models with a more intense SFE represent better the observed [Ce/O] trend in the inner regions, while models with a less efficient SFE describe the [Ce/O] behaviour in the outer regions. These GCE models also allow us to reproduce the present-day [Ce/O] gradient.

To conclude, our results show a strong dependence of Ce on metallicity, stellar age, and position in the Galactic disc. Moreover, Ce, a heavy s-process element, is mainly produced by low-mass AGB stars. Their longer lifetime implies a delayed ejection with respect to intermediate and massive stars, and a late contribution to the Galactic chemical evolution. Finally, the uncertainties on s-process yields due to the metallicity dependence, treatment of the ^{13}C-pocket, convection, mass-loss rates, among other factors, require further investigation. These investigations are likely to shed light on the trends of Ce abundances, and those of the other s-process elements, with age.

References

Abdurro'uf, Accetta, K., Aerts, C., et al. 2022, ApJS, 259, 35
Adibekyan, V. Z., Sousa, S. G., Santos, N. C., et al. 2012, A&A, 545, A32
Anders, F., Chiappini, C., Minchev, I., et al. 2017, A&A, 600, A70
Anders, F., Chiappini, C., Santiago, B. X., et al. 2018, A&A, 619, A125
Anguiano, B., Majewski, S. R., Allende-Prieto, C., et al. 2018, A&A, 620, A76
Baglin, A., Auvergne, M., Boisnard, L., et al. 2006, in 36th COSPAR Scientific Assembly, 36, 3749
Bailer-Jones, C. A. L., Rybizki, J., Fouesneau, M., Demleitner, M., & Andrae, R. 2021, AJ, 161, 147
Battino, U., Tattersall, A., Lederer-Woods, C., et al. 2019, MNRAS, 489, 1082
Binney, J., & Tremaine, S. 2008, Galactic Dynamics: Second Edition (Princeton University Press)
Bisterzo, S., Travaglio, C., Gallino, R., Wiescher, M., & Käppeler, F. 2014, ApJ, 787, 10
Borucki, W. J., Koch, D., Basri, G., et al. 2010, Science, 327, 977
Bovy, J. 2015, ApJS, 216, 29
Busso, M., Gallino, R., Lambert, D. L., Travaglio, C., & Smith, V. V. 2001, ApJ, 557, 802
Casagrande, L., & VandenBerg, D. A. 2014, MNRAS, 444, 392
Casagrande, L., & VandenBerg, D. A. 2018a, MNRAS, 479, L102
Casagrande, L., & VandenBerg, D. A. 2018b, MNRAS, 475, 5023
Casali, G., Magrini, L., Tognelli, E., et al. 2019, A&A, 629, A62
Casali, G., Spina, L., Magrini, L., et al. 2020, A&A, 639, A127
Casamiquela, L., Carrera, R., Jordi, C., et al. 2016, MNRAS, 458, 3150
Casamiquela, L., Soubiran, C., Jofré, P., et al. 2021, A&A, 652, A25
Cescutti, G., & Chiappini, C. 2014, A&A, 565, A51
Cescutti, G., Chiappini, C., Hirschi, R., Meynet, G., & Frischknecht, U. 2013, A&A, 553, A51
Cescutti, G., Chiappini, C., & Hirschi, R. 2018, in Rediscovering Our Galaxy, eds. C. Chiappini, I. Minchev, E. Starkenburg, & M. Valentini, 334, 94
Chaplin, W. J., & Miglio, A. 2013, ARA&A, 51, 353
Chiappini, C. 2013, Astron. Nachr., 334, 595
Chiappini, C., Matteucci, F., & Romano, D. 2001, ApJ, 554, 1044
Chiappini, C., Frischknecht, U., Meynet, G., et al. 2011, Nature, 472, 454
Contursi, G., de Laverny, P., Recio-Blanco, A., et al. 2023, A&A, 670, A106
Cristallo, S., Straniero, O., Gallino, R., et al. 2009, ApJ, 696, 797
Cristallo, S., Piersanti, L., Straniero, O., et al. 2011, ApJS, 197, 17
Cristallo, S., Straniero, O., Piersanti, L., & Gobrecht, D. 2015, ApJS, 219, 40
da Silva, L., Girardi, L., Pasquini, L., et al. 2006, A&A, 458, 609
da Silva, R., Porto de Mello, G. F., & Milone, A. C. 2012, A&A, 542, A84
Delgado Mena, E., Moya, A., Adibekyan, V., et al. 2019, A&A, 624, A78
Donor, J., Frinchaboy, P. M., Cunha, K., et al. 2020, AJ, 159, 199
Elsworth, Y., Themeßl, N., Hekker, S., & Chaplin, W. 2020, Res. Notes Am. Astron. Soc., 4, 177
Feltzing, S., Howes, L. M., McMillan, P. J., & Stonkutė, E. 2017, MNRAS, 465, L109
Foreman-Mackey, D., Hogg, D. W., Lang, D., & Goodman, J. 2013, PASP, 125, 306
Frischknecht, U., Hirschi, R., Pignatari, M., et al. 2016, MNRAS, 456, 1803
Gaia Collaboration (Brown, A. G. A., et al.) 2021, A&A, 649, A1
Gallino, R., Arlandini, C., Busso, M., et al. 1998, ApJ, 497, 388

García Pérez, A. E., Allende Prieto, C., Holtzman, J. A., et al. 2016, AJ, 151, 144

Gilliland, R. L., Brown, T. M., Christensen-Dalsgaard, J., et al. 2010, PASP, 122, 131

Green, G. 2018, J. Open Source Softw., 3, 695

Green, G. M., Schlafly, E., Zucker, C., Speagle, J. S., & Finkbeiner, D. 2019, ApJ, 887, 93

Grisoni, V., Spitoni, E., Matteucci, F., et al. 2017, MNRAS, 472, 3637

Grisoni, V., Spitoni, E., & Matteucci, F. 2018, MNRAS, 481, 2570

Grisoni, V., Cescutti, G., Matteucci, F., et al. 2020, MNRAS, 492, 2828

Hayes, C. R., Masseron, T., Sobeck, J., et al. 2022, ApJS, 262, 34

Hekker, S., & Johnson, J. A. 2019, MNRAS, 487, 4343

Howell, S. B., Sobeck, C., Haas, M., et al. 2014, PASP, 126, 398

Huber, P. J. 1964, Ann. Math. Stat., 35, 73

Jofré, P., Jackson, H., & Tucci Maia, M. 2020, A&A, 633, L9

Jurić, M., Ivezić, Ž., Brooks, A., et al. 2008, ApJ, 673, 864

Karakas, A. I., & Lugaro, M. 2016, ApJ, 825, 26

Kass, R. E., & Raftery, A. E. 1995, J. Am. Stat. Assoc., 90, 773

Kobayashi, C., Umeda, H., Nomoto, K., Tominaga, N., & Ohkubo, T. 2006, ApJ, 653, 1145

Lindegren, L., Bastian, U., Biermann, M., et al. 2021, A&A, 649, A4

Lugaro, M., Herwig, F., Lattanzio, J. C., Gallino, R., & Straniero, O. 2003, ApJ, 586, 1305

Mackereth, J. T., Miglio, A., Elsworth, Y., et al. 2021, MNRAS, 502, 1947

Magrini, L., Spina, L., Randich, S., et al. 2018, A&A, 617, A106

Magrini, L., Vescovi, D., Casali, G., et al. 2021, A&A, 646, L2

Maiorca, E., Randich, S., Busso, M., Magrini, L., & Palmerini, S. 2011, ApJ, 736, 120

Majewski, S. R., Schiavon, R. P., Frinchaboy, P. M., et al. 2017, AJ, 154, 94

Martig, M., Fouesneau, M., Rix, H.-W., et al. 2016, MNRAS, 456, 3655

Masseron, T., & Gilmore, G. 2015, MNRAS, 453, 1855

Masseron, T., Merle, T., & Hawkins, K. 2016, Astrophysics Source Code Library [record ascl:1605.004]

Matteucci, F. 2021, A&ARv, 29, 5

Matteucci, F., & Francois, P. 1989, MNRAS, 239, 885

Meynet, G., & Maeder, A. 2002, A&A, 390, 561

Miglio, A., Chiappini, C., Mackereth, J. T., et al. 2021, A&A, 645, A85

Mikolaitis, Š., Hill, V., Recio-Blanco, A., et al. 2014, A&A, 572, A33

Morel, T., Creevey, O. L., Montalbán, J., Miglio, A., & Willett, E. 2021, A&A, 646, A78

Myers, N., Donor, J., Spoo, T., et al. 2022, AJ, 164, 85

Ness, M., Hogg, D. W., Rix, H. W., et al. 2016, ApJ, 823, 114

Nissen, P. E. 2015, A&A, 579, A52

Nissen, P. E., Christensen-Dalsgaard, J., Mosumgaard, J. R., et al. 2020, A&A, 640, A81

Pignatari, M., Gallino, R., Meynet, G., et al. 2008, ApJ, 687, L95

Pignatari, M., Gallino, R., Heil, M., et al. 2010, ApJ, 710, 1557

Prantzos, N., Abia, C., Limongi, M., Chieffi, A., & Cristallo, S. 2018, MNRAS, 476, 3432

Randich, S., Gilmore, G., Magrini, L., et al. 2022, A&A, 666, A121

Razera, R., Barbuy, B., Moura, T. C., et al. 2022, MNRAS, 517, 4590

Rendle, B. M., Miglio, A., Chiappini, C., et al. 2019, MNRAS, 490, 4465

Ricker, G. R., Winn, J. N., Vanderspek, R., et al. 2014, SPIE Conf. Ser., 9143, 914320

Ricker, G. R., Winn, J. N., Vanderspek, R., et al. 2015, J. Astron. Telescopes Instrum. Syst., 1, 014003

Rodrigues, T. S., Bossini, D., Miglio, A., et al. 2017, MNRAS, 467, 1433

Sales-Silva, J. V., Daflon, S., Cunha, K., et al. 2022, ApJ, 926, 154

Schönrich, R., & Binney, J. 2009, MNRAS, 399, 1145

Schönrich, R., Binney, J., & Dehnen, W. 2010, MNRAS, 403, 1829

Sellwood, J. A., & Binney, J. J. 2002, MNRAS, 336, 785

Skrutskie, M. F., Cutri, R. M., Stiening, R., et al. 2006, AJ, 131, 1163

Slumstrup, D., Grundahl, F., Brogaard, K., et al. 2017, A&A, 604, L8

Sneden, C., Cowan, J. J., & Gallino, R. 2008, ARA&A, 46, 241

Spina, L., Meléndez, J., Karakas, A. I., et al. 2018, MNRAS, 474, 2580

Spitoni, E., Verma, K., Silva Aguirre, V., et al. 2021, A&A, 647, A73

Tailo, M., Corsaro, E., Miglio, A., et al. 2022, A&A, 662, L7

Tautvaišienė, G., Viscasillas Vázquez, C., Mikolaitis, Š., et al. 2021, A&A, 649, A126

Vescovi, D., Cristallo, S., Busso, M., & Liu, N. 2020, ApJ, 897, L25

Viscasillas Vázquez, C., Magrini, L., Casali, G., et al. 2022, A&A, 660, A135

Appendix A: Mock data

We generated mock data using a uniform distribution for [Fe/H], between −0.5 and 0.3 dex, and a truncated Gaussian for the age distribution, with a median of 7 Gyr, bound between 1 and 12 Gyr, and a σ-value of 3.5 Gyr. These choices aim to broadly reproduce the observed distributions.
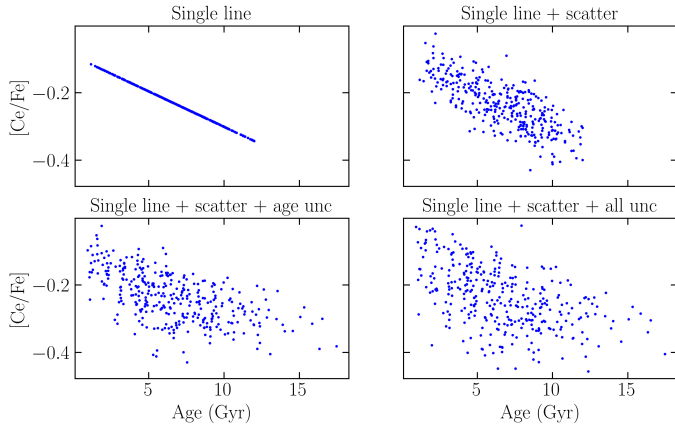

Fig. A.1. Distribution of mock data using single-line model. The top right panel is the model including the intrinsic scatter, the bottom left panel is the model with intrinsic scatter and age uncertainties, the bottom right panel is the model including the intrinsic scatter and all uncertainties.

Then we defined a function to generate [Ce/Fe] based on a single-line model (see Sect. 5.1). Then we added a scatter, and afterwards the uncertainties on [Fe/H], [Ce/Fe], and relative age: $\sigma_{[Fe/H]}$ = 0.05 dex; $\sigma_{[Ce/Fe]}$ = 0.05 dex; σ_{Age} = 30% (see Fig. A.1).

Finally, we performed the MCMC simulations applying the broken-line and the single-line model to the data (with scatter and uncertainties included) generated using a single-line. We did this to understand which of the two models can reproduce the mock data better. If the broken-line reproduces the mock data better, this means the change in slope in the [Ce/Fe]–age plane that we see in our data is due to the larger age uncertainties of older stars. If, instead, the single-line reproduces the observational data better, this implies the change in slope might be due to the Galactic evolution.

To determine which model fits the mock data better, we used the Bayesian information criterion (BIC) parameter. The model with the lowest BIC is the most reasonable one. We obtained a BIC of −803.13 for the broken-line and of −813.68 for the single-line. Following the rules by Kass & Raftery (1995), we can thus compute $\Delta BIC = BIC_i − BIC_{min}$. Given i models, the magnitude of the ΔBIC can be interpreted as evidence against a candidate model being the best model. The rules of thumb are the following: (i) less than 2, it is barely worth mentioning; (ii) between 2 and 6, the evidence against the candidate model is positive; (iii) between 6 and 10, the evidence against the candidate model is strong; (iv) greater than 10, the evidence is very strong. In our case the ΔBIC is larger than 10. This shows that the single-line model is the most reasonable one.

Appendix B: Additional figures

In this Appendix we present some additional figures for a better understanding of our work. Figure B.1 displays the [Ce/Fe] uncertainties distributions for the *Kepler*, TESS, and K2 stars in different bins of age, while Fig. B.2 shows the [Ce/α]–age planes for the three data samples in different bins of R_g. The three different lines in Fig. B.2 represent the [Ce/α] average in three different bins of metallicity: [Fe/H] < −0.1, −0.1 ≤ [Fe/H] ≤ +0.1, [Fe/H] > +0.1. For the K2 stars in the interval R_g < 5 kpc, we do not plot the [Ce/α] average because there are too few stars.
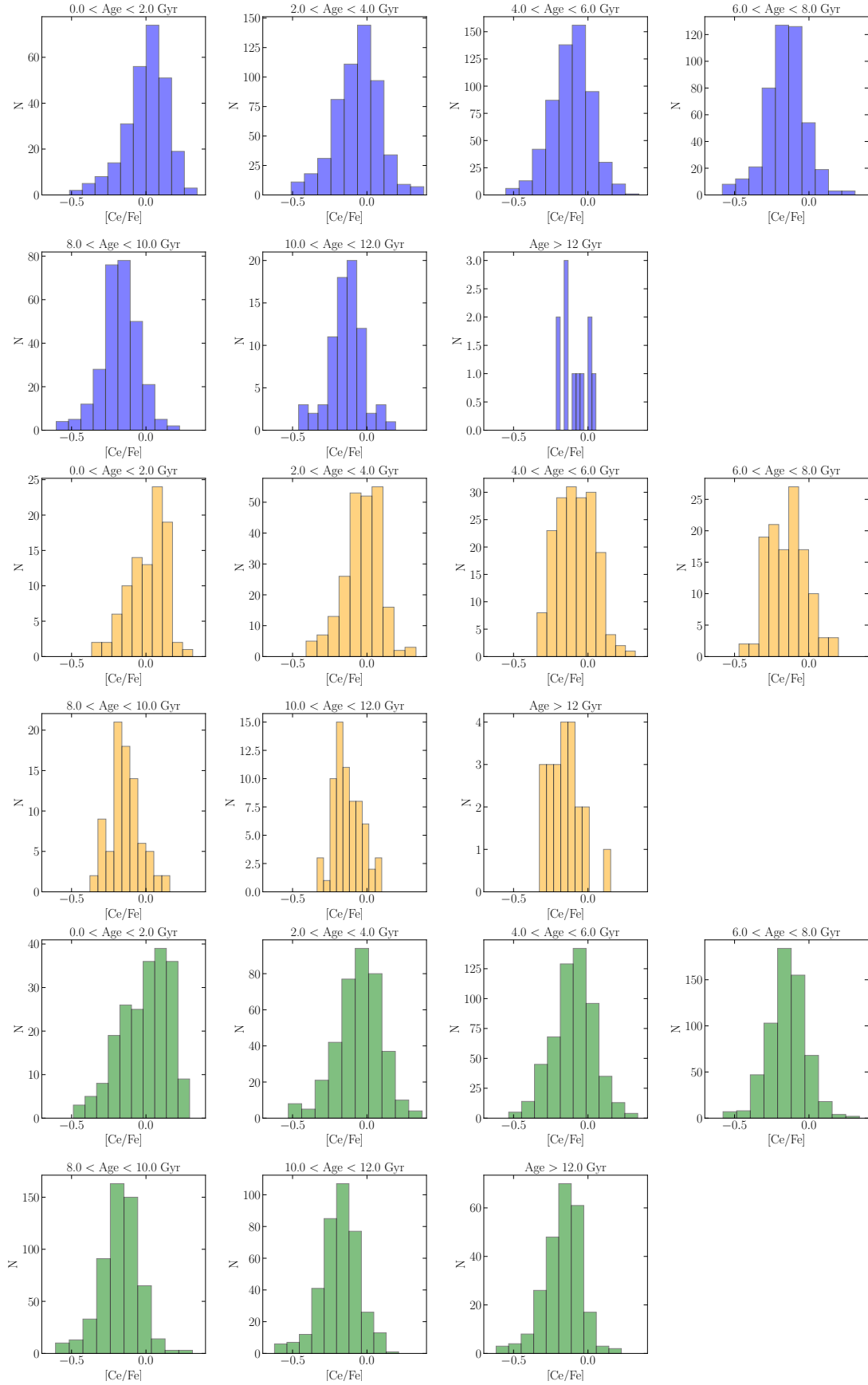
Fig. B.1. [Ce/Fe] distributions of the low-α sequences of *Kepler* (top, blue), TESS (middle, orange), and K2 (bottom, green) in different bins of stellar age.
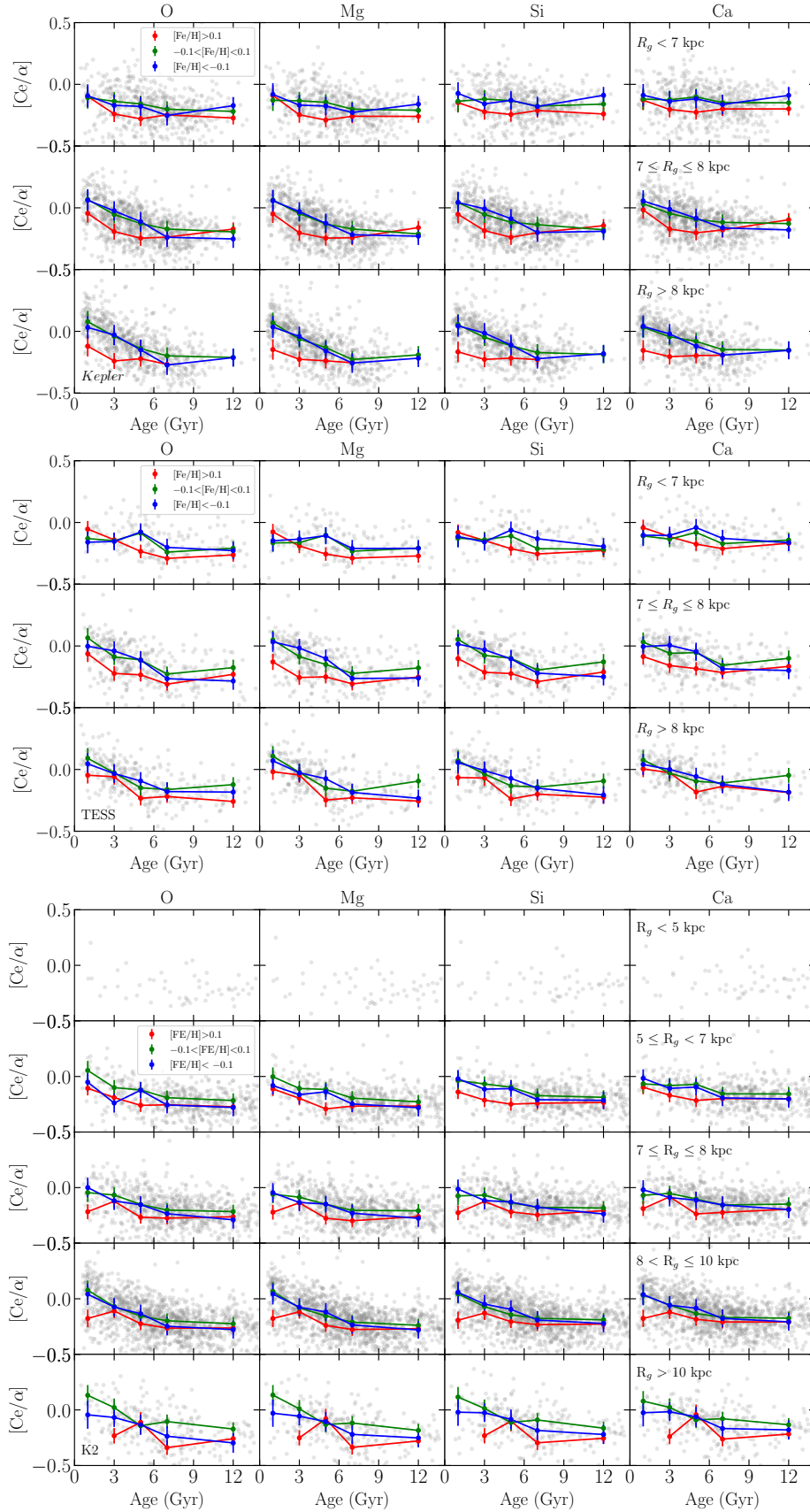
Fig. B.2. [Ce/α]–age planes for the low-α *Kepler* (top), TESS (middle), and K2 (bottom) stars in different bins of R_g. The three lines represent the [Ce/α] average in three different bins of metallicity: [Fe/H] < −0.1, −0.1 ≤ [Fe/H] ≤ +0.1, [Fe/H] > +0.1.